



The *R*-process Alliance: First Release from the Southern Search for *R*-process-enhanced Stars in the Galactic Halo*

Terese T. Hansen¹ , Erika M. Holmbeck^{2,3} , Timothy C. Beers^{2,3} , Vinicius M. Placco^{2,3} , Ian U. Roederer^{3,4} , Anna Frebel^{3,5} , Charli M. Sakari⁶ , Joshua D. Simon¹, and Ian B. Thompson¹

¹ The Observatories of the Carnegie Institution for Science, 813 Santa Barbara Street, Pasadena, CA 91101, USA; thansen@carnegiescience.edu

² Department of Physics, University of Notre Dame, Notre Dame, IN 46556, USA

³ Joint Institute for Nuclear Astrophysics—Center for the Evolution of the Elements (JINA-CEE), USA

⁴ Department of Astronomy, University of Michigan, 1085 S. University Avenue, Ann Arbor, MI 48109, USA

⁵ Department of Physics and Kavli Institute for Astrophysics and Space Research, Massachusetts Institute of Technology, Cambridge, MA 02139, USA

⁶ Department of Astronomy, University of Washington, Seattle, WA 98195-1580, USA

Received 2018 February 13; revised 2018 March 26; accepted 2018 March 27; published 2018 May 10

Abstract

The recent detection of a binary neutron star merger and the clear evidence of the decay of radioactive material observed in this event have, after 60 years of effort, provided an astrophysical site for the rapid neutron-capture (*r*-) process which is responsible for the production of the heaviest elements in our universe. However, observations of metal-poor stars with highly enhanced *r*-process elements have revealed abundance patterns suggesting that multiple sites may be involved. To address this issue, and to advance our understanding of the *r*-process, we have initiated an extensive search for bright ($V < 13.5$), very metal-poor ($[\text{Fe}/\text{H}] < -2$) stars in the Milky Way halo exhibiting strongly enhanced *r*-process signatures. This paper presents the first sample collected in the southern hemisphere using the echelle spectrograph on du Pont 2.5 m telescope at Las Campanas Observatory. We have observed and analyzed 107 stars with $-3.13 < [\text{Fe}/\text{H}] < -0.79$. Of those, 12 stars are strongly enhanced in heavy *r*-process elements (*r*-II), 42 stars show moderate enhancements of heavy *r*-process material (*r*-I), and 20 stars exhibit low abundances of the heavy *r*-process elements and higher abundances of the light *r*-process elements relative to the heavy ones (limited-*r*). This search is more successful at finding *r*-process-enhanced stars compared to previous searches, primarily due to a refined target selection procedure that focuses on red giants.

Key words: stars: abundances – stars: chemically peculiar – stars: Population II

Supporting material: machine-readable tables

1. Introduction

For more than 60 years, astronomers have searched for the astrophysical site of the heaviest elements in our universe—the elements produced by the rapid neutron-capture process (*r*-process), first described by Burbidge et al. (1957) and Cameron (1957). Neutron star mergers (NSMs) have long been proposed as sites for the *r*-process (Lattimer & Schramm 1974; Rosswog et al. 2014; Thielemann et al. 2017). This hypothesis was strongly supported by the discovery of Reticulum II, an ultra-faint dwarf galaxy highly enhanced in heavy *r*-process elements (Ji et al. 2016a; Roederer et al. 2016), and recently confirmed with the detection of gravitational waves from a NSM by LIGO (Abbott et al. 2017), where photometric and spectroscopic follow-up of the kilonova source SSS17a associated with GW170817 (Kilpatrick et al. 2017) exhibited clear evidence for the presence of unstable isotopes created by the *r*-process (Drout et al. 2017; Shappee et al. 2017).

However, it is not yet known if NSMs occur with sufficient frequency, produce sufficient amounts of *r*-process-element material, and if they are capable of producing the full mass range of *r*-process elements to be the sole source of the *r*-process elements in the universe, or whether additional sites are required (see, e.g., Côté et al. 2017). Other candidates for neutron-capture-element production in the early universe that are still not ruled out include jets in magneto-rotational supernovae (Jet-SNe; Cameron 2003; Winteler et al. 2012;

Nishimura et al. 2015; Mösta et al. 2017) and neutrino-driven winds in core-collapse supernovae (CCSNe; Arcones et al. 2007; Wanajo 2013; Thielemann et al. 2017). CCSNe are mainly believed to contribute to the light neutron-capture elements up to $Z = 56$, whereas some Jet-SN models produce the full mass range like the NSMs (Nishimura et al. 2015), while more recent models only produce the light elements (Mösta et al. 2017). However, although the abundance pattern produced by the Jet-SNe and NSMs may be similar, the timescales of the two events are quite different—massive stars explode on timescales of ~ 1 –10 Myr, while a few hundred Myr to a few Gyr are typically needed for NSMs to take place (Dominik et al. 2012).

Complementary to other efforts, progress toward solving this puzzle can be obtained by observations of very metal-poor (VMP; $[\text{Fe}/\text{H}] < -2$) and extremely metal-poor (EMP; $[\text{Fe}/\text{H}] < -3$) stars in the halo of the Milky Way, as such stars formed from gas polluted by one or only a few enrichment events, leaving a clear signature of the event(s) in the abundance patterns of these stars (Beers & Christlieb 2005; Frebel & Norris 2015).

Different types of *r*-process element abundance patterns exist at low metallicity. One group of stars exhibits enhancements of the heavy *r*-process elements with $Z \geq 56$. Europium (Eu; $Z = 63$) is used as a tracer of the *r*-process in these stars, as this element is almost entirely produced by the *r*-process at early times, and is the easiest of the heavy *r*-process elements to measure in optical spectra. These *r*-process-enhanced metal-poor stars are divided into two subclasses: the moderately enhanced *r*-I stars with $+0.3 \leq [\text{Eu}/\text{Fe}] \leq +1.0$, and the

* This paper includes data gathered with the 2.5 m du Pont telescope located at Las Campanas Observatory, Chile.

Table 1
Abundance Signatures for *r*-II, *r*-I, Limited-*r*, and CEMP-*r* Stars

Subclass	Abundances
<i>r</i> -II	$[\text{Eu}/\text{Fe}] > +1.0, [\text{Ba}/\text{Eu}] < 0$
<i>r</i> -I	$+0.3 \leq [\text{Eu}/\text{Fe}] \leq +1.0, [\text{Ba}/\text{Eu}] < 0$
limited- <i>r</i>	$[\text{Sr}/\text{Ba}] > +0.5, [\text{Eu}/\text{Fe}] < +0.3$
CEMP- <i>r</i> ^a	$[\text{C}/\text{Fe}] \geq +0.7, [\text{Eu}/\text{Fe}] > +0.3, [\text{Ba}/\text{Eu}] < 0$

Note.

^a The original definition of these stars only includes stars with $[\text{Eu}/\text{Fe}] > +1.0$ (Beers & Christlieb 2005), but we also include the *r*-I stars with carbon enhancement in this subclass.

highly enhanced *r*-II stars with $[\text{Eu}/\text{Fe}] > +1.0$ (Beers & Christlieb 2005). HE 1523–0901 (Frebel et al. 2007) is an example of a typical *r*-II star; HE 0524–2055 (Barklem et al. 2005) is a typical *r*-I star. A further division of the *r*-II subclass can be made based on the abundances of the actinide elements thorium and uranium. A subset of *r*-II stars exhibit an extra enhancement in these elements, the so-called “actinide-boost” stars such as CS 31082–001 (Hill et al. 2002).

A second group of stars exhibits low abundances of the heavy *r*-process elements ($[\text{Eu}/\text{Fe}] < +0.3$), and higher abundances of the light *r*-process elements, such as Strontium (Sr; $Z = 38$), relative to the heavy *r*-process elements ($[\text{Sr}/\text{Ba}] > +0.5$). These stars display the signature of an *r*-process that is limited by a small number of neutrons, with the consequence of producing primarily light *r*-process elements (see review by Frebel 2018); we therefore label these “limited-*r*” stars (previously they have been described as being enriched via the “weak” *r*-process or light element primary process). HD 122563 is the benchmark star of this group (Snedden & Parthasarathy 1983; Honda et al. 2006).

Finally, a number of the *r*-process-enhanced stars also show enhancements in carbon, the so-called carbon-enhanced metal-poor (CEMP)-*r* stars ($[\text{C}/\text{Fe}] \geq +0.7$ and $[\text{Eu}/\text{Fe}] > +0.3$). The first star of this type to be identified was CS 22892–052 (Snedden et al. 1994). The original definition of these stars only includes stars with $[\text{Eu}/\text{Fe}] > +1.0$ (Beers & Christlieb 2005), but we also include the *r*-I stars with carbon enhancement in this subclass. These four subclasses of *r*-process-enhanced stars, *r*-I, *r*-II, limited-*r*, and CEMP-*r* (summarized in Table 1) trace potential variations in *r*-process nucleosynthesis, as described in Frebel (2018), the dynamics of the progenitor objects, and/or in the mixing of the *r*-process-rich ejecta with the interstellar medium, at early and late times.

Over the past decades efforts have been made to systematically search for *r*-process-enhanced stars. Christlieb et al. (2004) and Barklem et al. (2005; HERES I and II, respectively) carried out a search for *r*-II stars in the halo by taking “snapshot” ($R \sim 20,000$ – $25,000$ and $S/N \sim 30$) spectra of 253 VMP and EMP stars with VLT/UVES. They selected targets from the Hamburg/ESO Survey (HES) brighter than $B \sim 16.5$, with $0.5 < B - V < 1.2$ and $[\text{Fe}/\text{H}] < -2.5$.⁷ This survey yielded 8 new *r*-II stars and 35 *r*-I stars, corresponding to frequencies of $\sim 3\%$ and $\sim 15\%$. A number of additional *r*-II

and *r*-I stars have been added to the tally by other authors (e.g., Honda et al. 2004; Frebel et al. 2007; Lai et al. 2008; Mashonkina et al. 2014; Roederer et al. 2014b), resulting in a total of ~ 30 *r*-II stars and ~ 125 *r*-I stars known in the halo today. For the limited-*r* stars, a search in the JINAbase for metal-poor stars shows that about 42 stars with a limited-*r*-process-element signature are known today (Abohalima & Frebel 2017).

Additionally, spectroscopic studies of Milky Way dwarf satellite galaxies have resulted in a number of *r*-II and *r*-I stars being discovered in these systems, most recently with the discovery of the ultra-faint dwarf (UFD) galaxy Reticulum II, where seven of nine stars analyzed exhibit large enhancements in *r*-process elements (Ji et al. 2016a, 2016b; Roederer et al. 2016). Hansen et al. (2017) also reported on the discovery of an *r*-I star in the UFD galaxy Tucana III. More luminous (and more massive) systems such as Ursa Minor and Draco also contain a number of *r*-process-enhanced stars (Shetrone et al. 2003; Aoki et al. 2007; Cohen & Huang 2009, 2010; Tsujimoto et al. 2017). Furthermore, many metal-poor globular clusters are *r*-process enhanced and contain a large number of *r*-I stars (Gratton et al. 2004). One *r*-II star with $[\text{Eu}/\text{Fe}] = +1.18$ has even been detected in M15 (Sobeck et al. 2011).

Some characteristics have been found for the neutron-capture-element abundance pattern of *r*-process-enhanced stars, such as the very robust pattern seen in *r*-I and *r*-II stars from Ba to Hf, matching that of the solar system *r*-process-abundance pattern in this range (Barklem et al. 2005; Siqueira Mello et al. 2014). However, the simple reality is that, once sliced into subsamples that highlight possibly contrasting behaviors among these stars, one loses the ability to statistically quantify the results with any precision. Furthermore, the majority of the currently known *r*-II stars are faint ($V > 13.5$), hence large amounts of telescope time are needed to obtain spectra with sufficient signal to noise (S/N) to derive abundances for a large number of neutron-capture elements in these stars.

To further advance our understanding of the *r*-process, we have established a collaboration known as the *R*-Process Alliance (RPA), which will combine observations, theory and modeling, and experiments from multiple fields to investigate different aspects of the *r*-process. The first goal in this effort is to carry out an extensive search for *r*-process-enhanced stars in our Galaxy, in order to increase the number of known *r*-II and limited-*r* stars from ~ 30 and ~ 40 , respectively, to ~ 100 – 125 each (we expect some 500 *r*-I stars to be discovered in the process as well), and thus compile a much larger “statistical” sample of such stars that is sufficiently bright to facilitate abundance determinations for a large number of neutron-capture elements.

This paper describes the first data sample from the southern hemisphere search. A second paper in this series (C. M. Sakari et al. 2018, in preparation) will present the first data sample from the northern hemisphere search. Another paper reporting on more southern hemisphere targets is currently being prepared. From this large-scale search effort, we have already found several interesting *r*-process-enhanced stars (see Section 2.2), as well as the first bona-fide CEMP-*r* + *s* star (Gull et al. 2018).

⁷ Note that the colors and metallicity estimates were obtained from the original survey plates and subsequent medium-resolution spectroscopic follow-up, respectively. As a result, the final temperature and metallicity range of the HERES sample stars were broader than originally intended.

2. Observations

2.1. Strategy

From the survey carried out by Barklem et al. (2005), the expected frequencies of *r*-II and *r*-I stars in the halo system are $\sim 3\%$ and $\sim 15\%$, respectively. Among the 1658 metal-poor stars in JINABase, 42 stars have abundances that match our limited-*r* definition, resulting in a frequency of $\sim 3\%$ for this subclass (Abohalima & Frebel 2017). This frequency of limited-*r* stars is a lower limit, as many candidates with high upper limits on their Eu abundance exist, and these could belong to the limited-*r* (or *r*-I) subclasses. However, it is clear that only a few stars belonging to this subclass have data available to facilitate abundance derivation for a large number of heavy neutron-capture elements. In order to significantly increase the number of known *r*-II and limited-*r* stars in the halo we need to obtain snapshot spectra for a large number of bright stars, which facilitate abundance determination for a large number of neutron-capture elements.

To achieve the first goal of the RPA, we plan to obtain snapshot spectra of ~ 2500 stars with $V \lesssim 13.5$ and $[\text{Fe}/\text{H}] \leq -2.0$ over both the southern and northern hemispheres using a variety of moderate- to large-aperture telescopes. Here we present the first sample, taken with the Echelle spectrograph at the Las Campanas Observatory du Pont 2.5 m telescope. In a second paper, we report on a similar effort carried out with the Apache Point Observatory 3.5 m telescope (C. M. Sakari et al. 2018, in preparation), with additional papers to follow.

Although several tens of thousands of candidate stars with $[\text{Fe}/\text{H}] < -2$ are now known (primarily from SDSS/SEGUE; Abazajian et al. 2009; Yanny et al. 2009), the great majority are too faint to efficiently obtain high-resolution data for a large number of stars in order to enable the determination of accurate abundances. Fortunately, a number of recent large surveys have provided suitably bright stars for consideration. Unfortunately, not all of these stars were known a priori to be VMP or EMP stars, thus Phase I of the RPA search for *r*-process-enhanced stars was to obtain medium-resolution validation data for those targets. These include stars from the RAVE survey (DR4; Kordopatis et al. 2013, DR5; Kunder et al. 2017) and the Best & Brightest Survey (B&B; Schlafman & Casey 2014). Note that, although the RAVE data releases provided estimates of metallicity for many bright stars, we have found that only about 60% of the stars from this survey with quoted $[\text{Fe}/\text{H}] < -2$ are in fact this metal-poor (Placco et al. 2018). We therefore decided to validate as many of these stars as possible before proceeding to the high-resolution observations. We have also included stars satisfying our selection criteria that already have had medium-resolution validation completed. These include stars from the HK Survey of Beers and collaborators (Beers et al. 1985, 1992; T. C. Beers et al. 2018, in preparation) or the Hamburg/ESO Survey of Christlieb and colleagues (Frebel et al. 2006; Christlieb et al. 2008; Beers et al. 2017; T. C. Beers et al. 2018, in preparation), from the SkyMapper Survey (Wolf et al. 2018), and (in particular in the northern hemisphere) G-K-giants selected from the LAMOST survey (T. C. Beers et al. 2018, in preparation). Stars from smaller lists of candidates from various programs carried out by members of our team were also included.

For Phase II, we selected targets with $V < 13.5$, $[\text{Fe}/\text{H}] < -2$, $4000 \text{ K} < T_{\text{eff}} < 5500 \text{ K}$, and not strongly enhanced in carbon, as validated by either extant medium-resolution spectra in our

possession or spectra that we gathered as part of Phase I of the search (see Placco et al. 2018 for a more detailed description of our target selection and determination of atmospheric parameters and $[\text{C}/\text{Fe}]$ using the n-SSPP, described by Beers et al. 2014). We then obtained snapshot high-resolution spectra with an S/N of ~ 30 at 4100 \AA and a resolving power $R \sim 25,000$. This can be achieved in a 1200 s exposure for a $V = 11.5$ star with a 2.5 m class telescope. Christlieb et al. (2004) and Barklem et al. (2005) established that such spectra are sufficient to detect (or derive meaningful upper limits on) an enhanced Eu line at 4129 \AA and an Sr line at 4077 \AA , for cool, VMP stars. We then derive C, Sr, Ba, and Eu abundances for these stars, which allow us to identify likely *r*-II, *r*-I, limited-*r*, and CEMP-*r* stars, following the selection criteria summarized in Table 1. When identifying *r*-II, *r*-I, and CEMP-*r* stars from spectra taken in Phase II, we also require that our selected stars satisfy $[\text{Ba}/\text{Eu}] < 0$ to ensure that the chemical composition of the stars is dominated by the *r*-process and not the slow neutron-capture process (*s*-process; Beers & Christlieb 2005).

Phase III of this effort, which is already underway, makes use of generally large-aperture telescopes in order to obtain much higher-quality “portrait” spectra (S/N ~ 100 at 3850 \AA ; $R \sim 50,000$ or higher) for all of the *r*-II and limited-*r* stars (and a subset of the *r*-I stars) identified during Phase II. Placco et al. (2017) reports on the first portrait spectrum taken during Phase III, for RAVE J203843.2–002333, a bright ($V = 12.7$), VMP ($[\text{Fe}/\text{H}] = -2.91$), *r*-II ($[\text{Eu}/\text{Fe}] = +1.64$, and $[\text{Ba}/\text{Eu}] = -0.81$) star originally identified during the RAVE survey; it is also only the fourth VMP/EMP star reported with a measured uranium abundance. In addition, RAVE J153830.9–180424, one of the most metal-rich *r*-II stars known in the Milky Way halo ($[\text{Fe}/\text{H}] = -2.09$), was recently identified in the northern hemisphere Phase-II search. The portrait spectrum of this star, and its elemental-abundance analysis, is presented in Sakari et al. (2018). The full set of portrait spectra will be analyzed and published in due course.

2.2. The Southern Hemisphere Search for *r*-Process-enhanced Stars

The first dataset on this program in the southern hemisphere was obtained during six nights in 2016 August, with the Echelle spectrograph on the du Pont 2.5 m telescope at the Las Campanas Observatory. During this run, we obtained spectra for 107 stars in the magnitude range of $10 < V < 13.5$ and with metallicities of $-3.13 < [\text{Fe}/\text{H}] < -0.79$ (note that these metallicities reflect the high-resolution abundance results, not those from Phase I). The spectra were obtained using the $1'' \times 4''$ slit and 2×2 on-chip binning, yielding a resolving power of $R \sim 25,000$, covering the wavelength range from 3860 to 9000 \AA . The data were reduced using the Carnegie Python Distribution⁸ (Kelson 1998, 2003; Illingworth et al. 2000). Radial velocities were measured from order-by-order cross-correlation of the target spectra with a spectrum of HD 213575, a radial-velocity standard star obtained during the run, using the *fxcor* task in IRAF.⁹ On average 17 orders in each spectrum were used for the correlation. We also estimated the S/N of each spectrum in the region of the 4129 \AA Eu line

⁸ <http://code.obs.carnegiescience.edu/>

⁹ IRAF is distributed by the National Optical Astronomy Observatory, which is operated by the Association of Universities for Research in Astronomy, Inc., under cooperative agreement with the NSF.

Table 2
Observation Log

Stellar ID	R.A.	Decl.	V mag ^a	MJD	Exp Time (s)	S/N 4129 Å	RV _{helio} (km s ⁻¹)	RV _{err} (km s ⁻¹)	Source	Other Identifier
J00002259–1302275	00 00 22.6	–13 02 27.5	12.9	57605.82086	296	17	–102.22	0.75	RAVE DR5	
				57607.81559	900	31	–102.24	1.25		
J00021222–2241388	00 02 12.2	–22 41 38.9	13.3	57606.83137	3600	24	+35.24	0.76	B&B	
J00021668–2453494	00 02 16.7	–24 53 49.5	13.5	57607.83983	3600	31	+78.82	0.49	B&B	
J00133067–1259594	00 13 30.7	–12 59 59.4	11.8	57608.80407	1000	31	–95.29	0.31	RAVE DR5	HE 0010–1316
J00233067–1631428	00 23 30.7	–16 31 43.2	12.3	57609.83271	1800	30	–8.78	0.55	RAVE DR5	
J00400685–4325183	00 40 06.9	–43 25 18.4	12.4	57606.86896	600	20	+48.93	0.74	RAVE DR5	HE 0037–4341
J00405260–5122491	00 40 52.6	–51 22 49.1	11.2	57609.81417	900	34	+123.11	0.21	RAVE DR5	CD–52 112
J00453930–7457294	00 45 39.3	–74 57 29.6	11.7	57608.82169	1200	31	–31.23	0.41	RAVE DR5	
J01202234–5425582	01 20 22.3	–54 25 58.2	12.6	57606.89108	2700	32	+68.00	0.85	RAVE DR5	
J01293113–1600454	01 29 31.1	–16 00 45.5	11.6	57609.84994	800	25	+139.47	0.30	RAVE DR5	CS 31082–001, BD–16 251
J01334657–2727374	01 33 46.6	–27 27 37.3	12.4	57608.85405	3600	42	–25.87	0.61	RAVE DR5	
J01425422–5032488	01 42 54.2	–50 32 48.9	11.4	57609.86360	1000	33	+158.15	0.17	RAVE DR5	
J01430726–6445174	01 43 07.3	–64 45 17.4	12.0	57610.86966	2100	35	+167.91	0.24	RAVE DR5	
J01451951–2800583	01 45 19.5	–28 00 58.4	11.7	57608.88461	1100	38	+34.89	0.28	RAVE DR5	
J01490794–4911429	01 49 07.9	–49 11 43.0	11.2	57610.80049	1200	42	+90.30	0.25	RAVE DR5	HE 0147–4926, CD–49 506
J01530024–3417360	01 53 00.2	–34 17 36.1	9.6	57606.91442	900	72	+22.81	0.33	RAVE DR5	HD 11582, CD–34 722
J02040793–3127556	02 04 07.9	–31 27 55.6	12.6	57607.90877	1900	37	+83.45	1.00	RAVE DR5	HE 0201–3142
J02165716–7547064	02 16 57.2	–75 47 06.6	11.9	57608.90250	1200	31	–5.80	0.27	RAVE DR5	
J02355867–6745520	02 35 58.7	–67 45 51.9	11.9	57610.82171	1800	23	+101.45	0.19	RAVE DR5	
J02401075–1416290	02 40 10.8	–14 16 29.9	13.1	57606.92573	600	19	+126.28	1.80	RAVE DR5	
J02412152–1825376	02 41 21.5	–18 25 37.8	11.7	57608.92031	1200	34	–108.51	0.24	RAVE DR5	
J02441479–5158241	02 44 14.8	–51 58 24.1	11.8	57609.88054	1400	32	+52.13	0.36	RAVE DR5	HE 0242–5211
J02462013–1518419	02 46 20.1	–15 18 41.9	12.5	57609.92227	600	20	+278.23	0.39	RAVE DR5	SDSS J024620.14–151842.0
J02500719–5145148	02 50 07.2	–51 45 15.1	12.4	57610.90069	2700	32	+310.48	0.22	RAVE DR5	
J03193531–3250433	03 19 35.3	–32 50 43.3	10.9	57610.84230	1200	52	+47.95	1.52	RAVE DR5	HE 0317–3301, CD–33 1173
J03563703–5838281	03 56 37.0	–58 38 28.1	11.4	57609.89703	900	22	+157.07	0.74	RAVE DR5	HE 0355–5847
J04121388–1205050	04 12 13.9	–12 05 05.1	12.9	57609.91101	900	19	+14.40	0.96	RAVE DR5	HE 0409–1212, CS 22169–0035
J13164824–2743351	13 16 48.2	–27 43 35.2	11.5	57605.50624	1200	32	+69.00	0.19	RAVE DR5	
J14033542–3335257	14 03 35.4	–33 35 25.7	11.5	57609.46903	600	29	+262.39	0.19	RAVE DR5	CD–33 9514
J14164084–2422000	14 16 40.8	–24 21 59.9	10.9	57609.47870	600	30	+0.84	0.26	RAVE DR5	
J14232679–2834200	14 23 26.8	–28 34 20.1	12.7	57607.48495	2700	33	+134.07	0.50	RAVE DR5	
J14301385–2317388	14 30 13.9	–23 17 38.7	12.0	57608.49486	400	25	+432.11	0.29	RAVE DR5	
J14325334–4125494	14 32 53.3	–41 25 49.5	11.1	57605.49093	1200	36	–227.92	0.14	B&B	
J14381119–2120085	14 38 11.2	–21 20 08.7	11.4	57609.49022	1000	26	+9.22	0.19	RAVE DR5	
J15260106–0911388	15 26 01.1	–09 11 38.7	11.1	57609.51084	400	22	–162.27	0.41	RAVE DR5	HE 1523–0901
J15271353–2336177	15 27 13.5	–23 36 17.7	10.8	57609.52091	900	45	+1.22	0.23	RAVE DR5	CD–23 12296
J15575183–0839549	15 57 51.8	–08 39 55.0	10.4	57609.53186	600	28	–21.32	0.15	RAVE DR5	BD–08 4115
J15582962–1224344	15 58 29.6	–12 24 34.4	12.3	57605.52399	1200	28	+83.08	0.42	RAVE DR5	
J16024498–1521016	16 02 45.0	–15 21 01.7	10.3	57606.55986	900	34	+101.26	0.45	RAVE DR5	BD–14 4336
J16080681–3215592	16 08 06.8	–32 15 59.3	12.7	57610.57131	2200	29	+163.49	0.41	B&B	
J16095117–0941174	16 09 51.2	–09 41 17.5	10.5	57608.50559	1000	53	+129.61	0.15	RAVE DR5	BD–09 4312
J16103106+1003055	16 10 31.1	+10 03 05.6	12.8	57607.52596	2400	33	–68.33	0.95	B&B	
J16184302–0630558	16 18 43.1	–06 30 55.5	12.1	57610.54438	1800	33	+80.91	0.43	RAVE DR5	
J17093199–6027271	17 09 32.0	–60 27 27.1	12.5	57605.54109	600	19	+332.85	0.37	RAVE DR5	
				57608.51985	600	25	+333.73	0.38		
J17094926–6239285	17 09 49.3	–62 39 28.6	12.6	57610.51453	2700	27	–50.98	0.30	RAVE DR5	

Table 2
(Continued)

Stellar ID	R.A.	Decl.	V mag ^a	MJD	Exp Time (s)	S/N 4129 Å	RV_{helio} (km s ⁻¹)	RV_{err} (km s ⁻¹)	Source	Other Identifier
J17124284–5211479	17 12 42.8	–52 11 47.9	13.1	57608.53750	1800	29	–26.56	1.28	B&B	
J17225742–7123000	17 22 57.4	–71 22 60.0	12.9	57605.55568	1200	21	+277.27	0.51	RAVE DR5	
				57607.54850	600	24	+278.07	1.08		
J17255680–6603395	17 25 56.8	–66 03 39.6	12.7	57609.55763	2700	27	+355.68	0.60	B&B	
J17273886–5133298	17 27 38.9	–51 33 30.0	12.1	57608.59039	1500	34	–219.14	0.41	B&B	
J17285930–7427532	17 28 59.3	–74 27 53.2	13.1	57607.57677	3600	33	+260.49	0.79	B&B	
J17334285–5121550	17 33 42.9	–51 21 55.1	12.5	57608.55990	1500	32	+105.35	0.24	B&B	
J17400682–6102129	17 40 06.8	–61 02 12.9	10.3	57606.57576	1200	43	+255.02	0.28	RAVE DR5	CD–60 6745
J17435113–5359333	17 43 51.1	–53 59 33.4	12.0	57605.57992	1000	28	+22.53	0.23	RAVE DR5	
J18024226–4404426	18 02 42.3	–44 04 42.6	12.6	57605.56963	300	18	–226.40	0.32	RAVE DR5	
				57608.57499	500	26	–226.06	1.72		
J18121045–4934495	18 12 10.5	–49 34 49.5	12.6	57608.61337	1800	34	+36.61	0.37	B&B	
J18285086–3434203	18 28 50.9	–34 34 20.4	12.7	57605.60844	1600	28	+22.73	0.33	B&B	
J18294122–4504000	18 29 41.2	–45 04 00.1	12.9	57606.59626	3600	22	–108.28	1.23	B&B	
J18362318–6428124	18 36 23.2	–64 28 12.5	12.5	57609.59046	2400	29	+16.21	0.32	B&B	
J18363613–7136597	18 36 36.1	–71 36 59.8	10.9	57605.59266	500	23	–68.32	0.20	RAVE DR5	
J18562774–7251331	18 56 27.7	–72 51 33.1	12.7	57610.60588	2800	26	+177.40	0.52	B&B	
J19014952–4844359	19 01 49.5	–48 44 35.9	12.5	57607.61450	2400	38	+133.36	0.32	B&B	
J19161821–5544454	19 16 18.2	–55 44 45.4	11.5	57605.62378	450	22	+46.58	0.29	RAVE DR5	
J19172402–4211240	19 17 24.0	–42 11 24.1	12.8	57605.64483	2700	34	+37.44	0.42	RAVE DR5	
J19173310–6628544	19 17 33.1	–66 28 54.5	13.1	57609.61946	4200	21	+62.18	0.52	B&B	
J19202070–6627202	19 20 20.7	–66 27 20.3	12.6	57607.64836	2700	35	+6.73	0.33	B&B	
J19215077–4452545	19 21 50.8	–44 52 54.6	11.4	57606.65080	3000	31	+3.53	0.50	RAVE DR5	
J19232518–5833410	19 23 25.2	–58 33 40.9	11.9	57606.63524	700	23	+125.88	0.57	RAVE DR5	
J19324858–5908019	19 32 48.6	–59 08 01.9	12.8	57608.63256	700	24	+303.44	0.50	RAVE DR5	
J19345497–5751400	19 34 55.0	–57 51 40.1	13.1	57608.64767	1300	27	–81.91	0.55	RAVE DR5	
J19494025–5424113	19 49 40.3	–54 24 11.2	12.7	57610.64351	3000	33	+61.07	0.49	RAVE DR5	
J19534978–5940001	19 53 49.8	–59 40 00.1	12.6	57608.66299	600	27	+216.45	0.55	RAVE DR5	CS 22873-0055
J19594558–2549075	19 59 45.5	–25 49 07.0	12.2	57609.50547	1200	22	–205.59	0.80	RAVE DR5	
J20093393–3410273	20 09 33.9	–34 10 27.3	11.8	57607.68078	2400	38	+27.24	0.30	RAVE DR5	
J20144608–5635300	20 14 46.1	–56 35 30.1	12.2	57605.67459	1200	23	–11.49	0.39	RAVE DR5	
J20165358–0503593	20 16 53.6	–05 03 59.3	12.5	57608.68904	2000	33	+27.34	0.72	B&B	
J20303339–2519500	20 30 33.4	–25 19 50.2	10.4	57605.68612	500	34	–57.98	0.13	RAVE DR5	CD–25 14822
J20313531–3127319	20 31 35.3	–31 27 31.9	13.6	57609.71514	1200	19	–223.19	2.15	RAVE DR5	
				57610.68591	3600	33	–222.53	0.16		
J20445584–2250597	20 44 55.9	–22 50 59.8	11.3	57608.71550	600	33	+51.86	0.16	RAVE DR5	
J20492765–5124440	20 49 27.7	–51 24 44.0	11.5	57605.69543	600	25	+24.56	0.20	RAVE DR5	
J20514971–6158008	20 51 49.7	–61 58 00.9	12.3	57609.67235	1500	27	–93.62	0.40	RAVE DR5	
J20542346–0033097	20 54 23.5	–00 33 09.8	11.7	57610.71914	1500	29	–61.92	0.25	RAVE DR5	
J20560913–1331176	20 56 09.1	–13 31 17.7	10.2	57607.70042	500	51	+123.45	0.11	RAVE DR5	HD 358059, BD–14 5890
J21023752–5316132	21 02 37.5	–53 16 13.3	12.9	57605.71525	2400	30	–3.34	0.48	B&B	
J21063474–4957500	21 06 34.7	–49 57 50.1	9.0	57608.72475	400	80	–44.13	0.29	RAVE DR5	HD 200654, CD–50 13237
J21064294–6828266	21 06 42.9	–68 28 26.7	12.8	57608.73613	900	27	–72.65	0.58	RAVE DR5	
J21091825–1310066	21 09 18.2	–13 10 06.2	10.7	57606.70093	550	32	–35.91	0.39	RAVE DR5	HD 358246
J21095804–0945400	21 09 58.1	–09 45 40.0	13.2	57606.71019	700	17	–20.59	1.58	RAVE DR5	
				57607.71303	700	24	–17.39	1.74		
				57608.75826	2200	27	–17.20	1.97		

Table 2
(Continued)

Stellar ID	R.A.	Decl.	V mag ^a	MJD	Exp Time (s)	S/N _o 4129 Å	RV_{helio} (km s ⁻¹)	RV_{err} (km s ⁻¹)	Source	Other Identifier
J21141350–5726363	21 14 13.5	–57 26 36.2	10.5	57607.72478	700	51	+158.37	0.08	RAVE DR5	V* AC Aqr, BD–02 5494
J21152551–1503309	21 15 25.5	–15 03 31.0	12.6	57609.74547	2400	22	–6.05	0.78	RAVE DR5	HE 2119–4653
J21162185–0213420	21 16 21.9	–02 13 42.0	10.2	57609.72698	400	21	–5.32	0.70	RAVE DR5	
J21224590–4641030	21 22 45.9	–46 41 03.1	12.3	57609.76828	1000	21	–100.75	0.45	RAVE DR5	
J21262525–2144243	21 26 25.3	–21 44 24.3	12.1	57606.73219	2700	32	–81.73	0.62	RAVE DR5	
J21291592–4236219	21 29 15.9	–42 36 22.0	13.0	57607.74035	1500	31	–143.15	0.43	RAVE DR5	
J21370807–0927347	21 37 08.1	–09 27 34.6	13.3	57605.74090	1500	21	–63.81	0.39	RAVE DR5	
J21513595–0543398	21 51 36.0	–05 43 39.8	10.0	57609.78191	800	35	–209.08	0.15	RAVE DR5	HD 207785, BD–06 5849
J22021636–0536483	22 02 16.4	–05 36 48.4	12.4	57609.79579	1200	21	–106.65	0.88	RAVE DR5	HE 2159–0551
J22163596+0246171	22 16 36.0	+02 46 17.1	12.7	57605.76641	1900	28	–98.32	0.41	B&B	
J22444701–5617540	22 44 47.0	–56 17 54.1	12.5	57606.75810	1200	24	–189.75	0.92	RAVE DR5	
J22492756–2238289	22 49 27.6	–22 38 29.0	12.0	57606.77131	1200	27	–1.42	0.43	RAVE DR5	
J22531984–2248555	22 53 19.9	–22 48 55.5	11.1	57607.78387	3600	71	–6.97	0.14	RAVE DR5	CD–23 17654
J22595884–1554182	22 59 58.8	–15 54 18.2	10.9	57606.79521	600	30	+19.37	0.51	RAVE DR5	BD–16 6190
J23022289–6833233	23 02 22.9	–68 33 23.3	11.6	57608.78529	1500	37	+136.05	0.23	RAVE DR5	
J23044914–4243477	23 04 49.1	–42 43 47.8	12.1	57605.79075	400	21	–278.06	0.50	RAVE DR5	HE 2302–4259
J23130003–4507066	23 13 00.0	–45 07 06.6	11.2	57610.78319	1200	39	–94.59	0.19	RAVE DR5	
J23265258–0159248	23 26 52.6	–01 59 24.8	11.2	57605.80255	1000	33	–215.33	0.31	RAVE DR5	HE 2324–0215, BD–02 5957
J23310716–0223301	23 31 07.2	–02 23 30.1	11.5	57606.80969	1500	29	–99.40	0.77	RAVE DR5	
J23362202–5607498	23 36 22.0	–56 07 49.8	12.9	57605.81383	300	17	+207.95	0.35	RAVE DR5	
				57607.81017	300	23	+209.55	0.53		

Note.^a RAVE DR5 V magnitudes are from Munari et al. (2014) and B&B are from Henden & Munari (2014)

(This table is available in machine-readable form.)

Table 3
Equivalent Widths of Fe I and Fe II Lines in Our Sample

Stellar ID	Species	λ (Å)	χ (eV)	$\log gf$	EW (mÅ)	$\log \epsilon$
J00002259–1302275	Fe I	4143.87	1.56	−0.51	133.30	5.04
J00002259–1302275	Fe I	4191.43	2.47	−0.67	94.10	5.28
J00002259–1302275	Fe I	4415.12	1.61	−0.62	117.10	4.78
J00002259–1302275	Fe I	4447.72	2.22	−1.34	94.40	5.59
J00002259–1302275	Fe I	4461.65	0.09	−3.19	122.20	5.73
⋮	⋮	⋮	⋮	⋮	⋮	⋮
J00002259–1302275	Fe I	6593.87	2.43	−2.42	30.50	5.44
J00002259–1302275	Fe I	6750.15	2.42	−2.62	43.30	5.87
J00002259–1302275	Fe II	4522.63	2.84	−1.99	83.00	5.35
J00002259–1302275	Fe II	4620.52	2.83	−3.19	74.20	6.33
J00002259–1302275	Fe II	4923.93	2.89	−1.21	87.50	4.68
J00002259–1302275	Fe II	5234.63	3.22	−2.18	37.00	4.97
J00002259–1302275	Fe II	5316.62	3.15	−1.78	94.10	5.65
J00002259–1302275	Fe II	6432.68	2.89	−3.71	34.70	6.04
J00021222–2241388	Fe I	4021.87	2.67	−0.73	84.24	5.43
J00021222–2241388	Fe I	4127.78	3.28	−1.61	18.42	5.55
J00021222–2241388	Fe I	4132.90	2.84	−0.92	58.74	5.22
J00021222–2241388	Fe I	4154.50	2.83	−0.69	76.67	5.41
⋮	⋮	⋮	⋮	⋮	⋮	⋮

(This table is available in its entirety in machine-readable form.)

by taking the square root of the total counts in the continuum, converted to photons by multiplying with the CCD gain = $1.05 \text{ e}^-/\text{DN}$. Table 2 lists the observed targets with R.A., decl., V magnitude, MJD, exposure time, S/N at 4129 Å , heliocentric radial velocity (RV_{helio}) and its associated error, the source catalog from which we originally selected each target, and additional common identifiers for the stars.

3. Stellar-parameter Derivations and Abundance Analysis

3.1. Parameters

We derive 1D LTE stellar parameters for our program stars from equivalent-width measurements of a large number of Fe I and Fe II lines, using the 2017 version of MOOG (Snedden 1973), including Rayleigh scattering treatment as described by Sobeck et al. (2011).¹⁰ The number of Fe lines used for the analysis ranges from 28 to 140 for Fe I and 6 to 27 for Fe II, with a mean of 86 and 15 lines used per spectrum, respectively. Equivalent widths of Fe I and Fe II lines measured for the individual stars, along with the wavelength (λ), excitation potential (χ), oscillator strength ($\log gf$), and derived abundances ($\log \epsilon$) for the lines, are listed in Table 3. Effective temperatures (T_{eff}) were derived by ensuring excitation equilibrium for the Fe I-line abundances. Spectroscopic derivation of stellar parameters using non-local thermodynamic equilibrium (NLTE) corrected Fe abundances has been found to agree better with photometric temperatures than what is found from LTE spectroscopic temperatures (Ezzeddine et al. 2017). We therefore place these initial temperatures on a photometric scale, correcting for the offset between spectroscopic and photometric temperature scales using the following

relation from Frebel et al. (2013):

$$T_{\text{eff, corrected}} = T_{\text{eff, initial}} - 0.1 \times T_{\text{eff, initial}} + 670.$$

The shift in temperature varies from 25 K for the hottest stars to 265 K for the coolest stars, with a mean shift of 208 K, owing to the predominantly low-temperature range of the sample. Surface gravities ($\log g$) were derived through ionization equilibration by ensuring agreement between abundances derived from Fe I and Fe II lines. Microturbulent velocities (ξ) were determined by removing any trend inline abundances with reduced equivalent widths for both Fe I and Fe II lines. Final parameters are listed in Table 4. We adopt an uncertainty of 150 K on T_{eff} , which reflects the uncertainty in the spectroscopically determined T_{eff} and a possible scale error from the application of the above relation. The standard deviation of the derived Fe I abundances varies from 0.09 dex to 0.28 dex, with a mean of 0.16 dex. Based on this value and the uncertainty in T_{eff} , we estimate uncertainties of 0.3 dex for $\log g$ and 0.3 km s^{-1} for ξ . Figure 1 shows the derived gravities as a function of effective temperature for the sample stars. Over-plotted are four Y^2 isochrones with $[\alpha/\text{Fe}] = +0.4$, age 12 Gyr, and $[\text{Fe}/\text{H}] = -2.0, -2.5, -3.0$, and -3.5 (Demarque et al. 2004). As the stars are selected to be bright and cool they mostly occupy the upper portion of the giant branch in this diagram. Four stars that are somewhat hotter than the rest of the sample were also observed, mainly because they were bright and/or due to the lack of other available targets in the appropriate R.A. range. Some of our stars also turned out to be more metal-rich than our initial selection criteria. This is mainly because not quite all of the targets initially chosen passed through the Phase I medium-resolution vetting process described in Section 2.1. A separate paper will address the differences in stellar parameters determined from the medium- and high-resolution spectra, respectively.

¹⁰ <https://github.com/alexji/moog17scat>

Table 4
Stellar Parameters

Stellar ID	T_{eff} (K)	$\log g$	[Fe/H]	$\sigma_{[\text{Fe}/\text{H}]}$ (dex)	$N(\text{Fe I})$	$N(\text{Fe II})$	ξ (km s^{-1})
J00002259–1302275	4576	2.12	−2.90	0.21	58	6	2.12
J00021222–2241388	5035	2.09	−2.19	0.19	107	13	1.85
J00021668–2453494	5020	1.73	−1.81	0.19	85	19	1.85
J00133067–1259594	4405	0.50	−2.82	0.17	71	14	2.60
J00233067–1631428	5382	3.04	−2.45	0.14	87	10	1.74
J00400685–4325183	4630	1.16	−2.55	0.21	64	9	2.75
J00405260–5122491	5689	4.51	−2.11	0.09	97	11	1.61
J00453930–7457294	4947	2.01	−2.00	0.16	115	22	1.90
J01202234–5425582	5125	2.53	−2.11	0.16	104	22	1.75
J01293113–1600454	4876	1.80	−2.81	0.12	74	14	2.13
J01334657–2727374	5227	2.79	−1.60	0.15	56	7	1.95
J01425422–5032488	5132	2.65	−2.09	0.12	122	20	1.55
J01430726–6445174	4590	0.92	−3.00	0.12	97	13	2.12
J01451951–2800583	4495	0.67	−2.80	0.15	69	20	2.10
J01490794–4911429	4682	0.93	−2.94	0.11	78	21	1.95
J01530024–3417360	5323	3.26	−1.50	0.13	132	21	1.40
J02040793–3127556	4550	0.92	−3.08	0.17	105	20	2.35
J02165716–7547064	4543	0.71	−2.50	0.14	90	16	2.44
J02355867–6745520	4653	0.91	−1.55	0.20	58	14	2.04
J02401075–1416290	6070	4.45	−0.79	0.19	47	16	0.80
J02412152–1825376	4405	0.80	−2.17	0.14	71	19	1.90
J02441479–5158241	4869	1.87	−2.93	0.13	86	16	1.69
J02462013–1518419	4879	1.80	−2.71	0.17	69	13	2.35
J02500719–5145148	4707	1.40	−2.20	0.20	115	23	2.30
J03193531–3250433	6311	3.05	−2.93	0.17	30	7	0.81
J03563703–5838281	4450	0.70	−2.87	0.16	68	12	2.60
J04121388–1205050	4658	0.95	−2.73	0.16	29	11	2.58
J13164824–2743351	4990	2.24	−1.61	0.17	127	20	1.50
J14033542–3335257	4889	1.75	−2.71	0.14	132	15	1.77
J14164084–2422000	4540	0.57	−2.73	0.13	77	23	1.95
J14232679–2834200	5200	2.66	−1.90	0.19	100	12	1.65
J14301385–2317388	4490	1.25	−1.40	0.16	92	18	2.40
J14325334–4125494	5020	2.39	−2.79	0.16	108	12	1.80
J14381119–2120085	4608	1.20	−2.21	0.20	109	18	2.20
J15260106–0911388	4499	0.76	−2.83	0.16	81	14	2.41
J15271353–2336177	5882	4.01	−2.15	0.12	130	17	1.35
J15575183–0839549	4730	1.88	−1.49	0.16	109	18	1.87
J15582962–1224344	5125	1.52	−2.54	0.16	105	22	2.35
J16024498–1521016	5240	3.16	−1.80	0.17	94	22	1.65
J16080681–3215592	4680	1.27	−2.07	0.16	119	23	1.98
J16095117–0941174	4556	0.68	−2.82	0.12	86	21	2.18
J16103106+1003055	5370	2.60	−2.43	0.19	64	6	2.05
J16184302–0630558	5407	1.67	−2.60	0.10	66	16	2.19
J17093199–6027271	4547	0.77	−2.48	0.20	70	13	2.71
J17094926–6239285	4585	0.90	−2.51	0.15	73	14	2.00
J17124284–5211479	4750	1.15	−2.78	0.19	74	15	2.00
J17225742–7123000	5080	2.67	−2.42	0.18	58	12	0.70
J17255680–6603395	4686	0.69	−2.59	0.11	80	14	2.38
J17273886–5133298	4992	1.38	−1.78	0.14	95	22	1.91
J17285930–7427532	4900	1.61	−2.04	0.17	74	13	1.80
J17334285–5121550	4899	1.18	−1.91	0.14	104	22	2.08
J17400682–6102129	4880	1.78	−2.24	0.16	107	18	2.08
J17435113–5359333	5080	1.65	−2.24	0.16	124	20	2.10
J18024226–4404426	4701	1.60	−1.55	0.18	88	14	2.17
J18121045–4934495	4436	0.76	−3.02	0.14	66	13	2.95
J18285086–3434203	4630	1.12	−2.46	0.15	118	17	2.15
J18294122–4504000	4700	1.25	−2.48	0.17	80	11	2.10
J18362318–6428124	4896	1.80	−2.57	0.10	97	19	1.95
J18363613–7136597	4650	0.65	−2.52	0.16	77	20	2.45
J18562774–7251331	4709	1.08	−2.26	0.15	97	8	2.15
J19014952–4844359	4820	1.84	−1.87	0.16	94	9	1.75
J19161821–5544454	4450	0.65	−2.35	0.18	66	18	2.50
J19172402–4211240	4775	1.06	−2.61	0.15	119	18	2.40

Table 4
(Continued)

Stellar ID	T_{eff} (K)	$\log g$	[Fe/H]	$\sigma_{[\text{Fe}/\text{H}]}$ (dex)	$N(\text{Fe I})$	$N(\text{Fe II})$	ξ (km s ⁻¹)
J19173310–6628545	4498	1.05	–2.76	0.15	64	12	2.72
J19202070–6627202	4690	1.64	–2.10	0.18	111	17	1.70
J19215077–4452545	4450	0.10	–2.56	0.17	74	11	2.30
J19232518–5833410	5035	2.12	–2.08	0.18	82	8	2.05
J19324858–5908019	4540	1.92	–1.93	0.18	46	11	1.70
J19345497–5751400	4580	1.74	–2.46	0.14	28	7	2.50
J19494025–5424113	4486	0.91	–2.81	0.17	72	13	2.24
J19534978–5940001	4614	0.70	–2.79	0.16	66	13	2.41
J19594558–2549075	4540	0.79	–2.44	0.15	95	21	2.64
J20093393–3410273	4690	1.64	–2.10	0.18	111	17	1.70
J20144608–5635300	4765	1.19	–1.92	0.18	41	18	1.80
J20165357–0503592	4585	0.90	–2.89	0.18	88	10	2.90
J20303339–2519500	4315	0.60	–2.18	0.18	106	24	2.30
J20313531–3127319	4894	1.39	–2.43	0.14	82	13	1.83
J20445584–2250597	4366	1.00	–2.30	0.18	111	15	2.16
J20492765–5124440	4250	1.09	–2.47	0.19	80	11	2.60
J20514971–6158008	5285	3.13	–1.87	0.14	114	19	1.68
J20542346–0033097	4351	0.68	–2.78	0.20	82	11	2.64
J20560913–1331176	4780	1.60	–2.30	0.13	119	24	1.80
J21023752–5316132	5045	2.40	–2.44	0.19	72	13	1.95
J21063474–4957500	5238	2.82	–2.91	0.13	102	15	1.93
J21064294–6828266	5186	2.70	–2.76	0.19	43	10	2.90
J21091825–1310062	4855	1.42	–2.40	0.17	106	24	2.10
J21095804–0945400	4492	0.98	–2.73	0.16	57	10	2.11
J21141350–5726363	4690	1.21	–2.69	0.15	140	10	2.05
J21152551–1503309	4722	1.47	–2.06	0.17	68	18	2.00
J21162185–0213420	4390	0.73	–2.23	0.16	62	11	1.90
J21224590–4641030	4652	1.42	–2.96	0.14	67	14	2.78
J21262525–2144243	4450	1.09	–2.81	0.17	121	12	2.45
J21291592–4236219	4650	1.15	–2.48	0.19	96	18	2.10
J21370807–0927347	4470	0.99	–2.46	0.18	84	14	2.05
J21513595–0543398	4530	0.66	–2.46	0.15	99	27	2.21
J22021636–0536483	4668	0.93	–2.75	0.18	67	14	2.57
J22163596+0246171	4900	1.92	–2.37	0.18	131	10	1.85
J22444701–5617540	4495	1.41	–1.86	0.21	43	11	1.75
J22492756–2238289	4930	1.81	–1.82	0.19	78	10	2.35
J22531984–2248555	4720	1.59	–1.87	0.18	91	18	1.65
J22595884–1554182	4600	0.92	–2.64	0.16	91	17	2.55
J23022289–6833233	5063	2.29	–2.64	0.15	110	14	2.21
J23044914–4243477	4733	2.12	–2.43	0.28	70	13	1.25
J23130003–4507066	4612	0.95	–2.64	0.18	87	18	2.21
J23265258–0159248	4360	0.45	–3.13	0.16	82	21	2.40
J23310716–0223301	5050	1.70	–2.28	0.15	30	7	2.05
J23362202–5607498	4630	1.28	–2.06	0.20	38	14	2.15

(This table is available in machine-readable form.)

3.2. Abundances

As described in Section 2.1, we derive abundances for C, Sr, Ba, and Eu for the stars in our sample, which allows us to classify the stars as either *r*-I, *r*-II, limited-*r*, CEMP-*s*, CEMP-*r*, or non-*r*-process-enhanced. As the stars were preferentially selected not to exhibit carbon enhancement, we did not expect to find a large number of CEMP-*s* or CEMP-*r* stars, but nevertheless included carbon measurements in our analysis. A full abundance analysis of the stars will follow in future papers. All abundances are derived from spectral syntheses using MOOG2017 and α -enhanced ($[\alpha/\text{Fe}] = +0.4$) 1D LTE ATLAS9 model atmospheres (Castelli & Kurucz 2003). We used solar photosphere abundances from Asplund et al. (2009)

and line lists generated using the linemake package¹¹ (C. Sneden 2018, private communication), including molecular lines from CH, C₂, and CN (Brooke et al. 2013; Masseron et al. 2014; Ram et al. 2014; Sneden et al. 2014) and isotopic shift and hyperfine structure information for Ba and Eu (Lawler et al. 2001; Gallagher et al. 2010).

Carbon abundances are derived by fitting the CH *G*-band at 4313 Å and/or the C₂ Swan band at 5161 Å. Three Sr lines are available in our wavelength range at 4077, 4161, and 4215 Å. The 4077 Å line is very strong and is often saturated in our spectra; on the other hand, the 4161 Å is weak and severely

¹¹ <https://github.com/vmplacco/linemake>

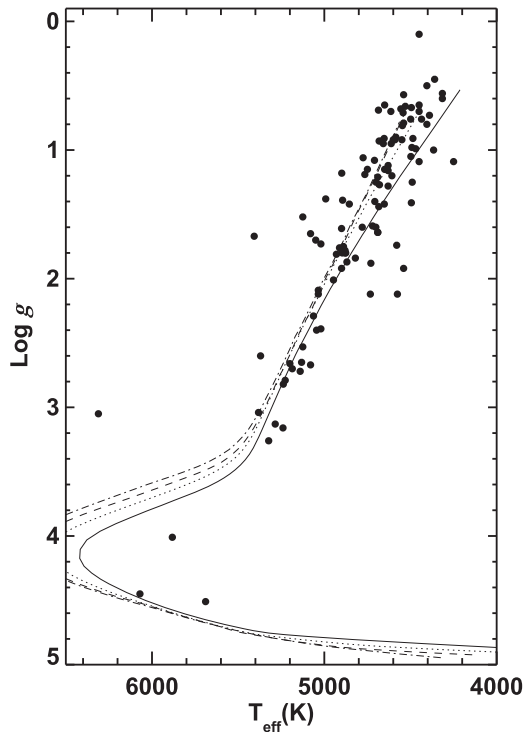


Figure 1. Surface gravity vs. effective temperature measurements for the sample stars, over-plotted with Y^2 isochrones for four different metallicities, solid: $[\text{Fe}/\text{H}] = -2.0$, dotted: $[\text{Fe}/\text{H}] = -2.5$, dashed: $[\text{Fe}/\text{H}] = -3.0$, and dotted-dashed: $[\text{Fe}/\text{H}] = -3.5$.

blended. Hence, our Sr abundances are primarily derived from the line at 4215 Å. This line can be blended with CN features in cool metal-poor stars. However, as our stars are chosen not to be enhanced in C, this was only a complication for a few spectra. Barium abundances are derived from three of the five Ba lines in our wavelength range at 5853, 6141, and 6496 Å. There are also Ba lines at 4554 and 4934 Å, but they were often saturated in these cool stars. Furthermore, the 4934 Å line is also blended with an Fe I feature for which the $\log gf$ value is poorly constrained; these two lines were disregarded for the final Ba abundance. For Eu, eight absorption lines are present in our spectral range at 3819, 3907, 4129, 4205, 4435, 4522, 6437, and 6645 Å. The 3819 and 3907 Å lines are in a region of our spectra with poor S/N, and the 4205, 4435, and 4522 Å features are heavily blended. Hence, our Eu abundances are mainly derived from the 4129 Å feature, and those at 6437 and 6645 Å, when detectable. Examples of the synthesis of Sr, Ba, and Eu lines used for the classification of a limited- r star, an r -I star, and an r -II star are shown in Figure 2.

4. Results

Final abundances derived for the 107 stars are listed in Table 5, along with their classifications based on these abundances. Table 6 lists the abundance uncertainties arising from stellar-parameter uncertainties, along with random errors, for the three stars representative of the stellar-parameter range of our sample. The random error is dominated by the uncertainty in continuum placement, and is estimated by deriving abundances for the lines with $\pm 1\sigma$ placement of continuum, based on our average S/N = 30. We computed these uncertainties by deriving abundances using atmosphere models varied by the uncertainty of the different parameters as

quoted in Section 3. These uncertainties are then added in quadrature, along with an additional estimated 0.05 dex random error.

4.1. Radial-velocity Variations

For nine of the stars in our sample, we find velocities differing from those reported by the RAVE survey DR5 (Kunder et al. 2017); these are listed in Table 7. The typical uncertainty of the radial velocities listed by RAVE DR5 is $< 2 \text{ km s}^{-1}$ (Kunder et al. 2017); the uncertainties of our radial velocities are typically $< 1 \text{ km s}^{-1}$ (see Table 2). We have therefore chosen to highlight stars for which the two measurements differ by more than 5 km s^{-1} . One of these, J225319.9–224856, is a CEMP- s star, a class of stars enhanced in both C and s -process elements, and primarily found in binary systems (Hansen et al. 2016). Four of these stars are r -II stars, while two are r -I stars, resulting in six possible binaries among the 50 new r -I and r -II stars discovered in our sample. Additionally, one of the r -II star rediscoveries, HE 1523–0901, is also known to be in a binary system, while the other, CS 31082–001, shows no sign of radial-velocity variation (Hansen et al. 2015). No binary information is available for the r -I rediscoveries. In total, this results in a binary frequency of $11.1 \pm 4.3\%$ (assuming binomial errors), which agrees with the binary frequency of $18 \pm 6\%$ previously found for r -process-enhanced stars (Hansen et al. 2011, 2015). This is a lower limit, given that, e.g., HE 1523–0901 has radial-velocity variations well below 1 km s^{-1} , a level that is not accounted for here. However, it is striking that four of our ten newly detected r -II stars are apparent binaries, whereas Hansen et al. (2015) only found one binary system among the nine r -II stars included in their sample. We note that none of the possible binary systems identified in Table 7 are double-lined spectroscopic binaries.

5. Discussion

5.1. Newly Identified r -process-enhanced Stars

Following the abundance-selection criteria listed in Table 1, we identify 12 r -II, 39 r -I, 20 limited- r , and 3 CEMP- r stars among the 107 stars observed. The three CEMP- r stars all have an Eu enhancement in the r -I star Eu range, and therefore we include them in this group in the following figures and discussion. Two of the identified r -II stars are rediscoveries: J15260106–0911388 = HE 1523–0901 (Frebel et al. 2007) and J01293113–1600454 = CS 31082–001 (Hill et al. 2002). Two of the r -I stars are rediscoveries: J21063474–4957500 = HD 200654 (Roederer et al. 2014a) and J23265258–0159248 (Thanathibodee 2016). Thus, we have identified 10 new r -II stars and 37 new r -I stars. The frequencies of new r -process-enhanced stars are somewhat higher than was found by Barklem et al. (2005), who identified 8 r -II and 35 r -I stars in their sample of 253 stars. However, the stars in the sample of Barklem et al. (2005) are generally warmer and fainter than our targets, often impeding the detection of Eu and other neutron-capture elements if the target S/N is not reached for the data. Hence, a number of their non-detections may not be real, but rather, a result of higher stellar temperature, low S/N, or a combination of both.

Specific searches for stars that exhibit a limited- r -process signature have not been carried out in the past, although multiple works have recognized the existence of these stars (e.g.,

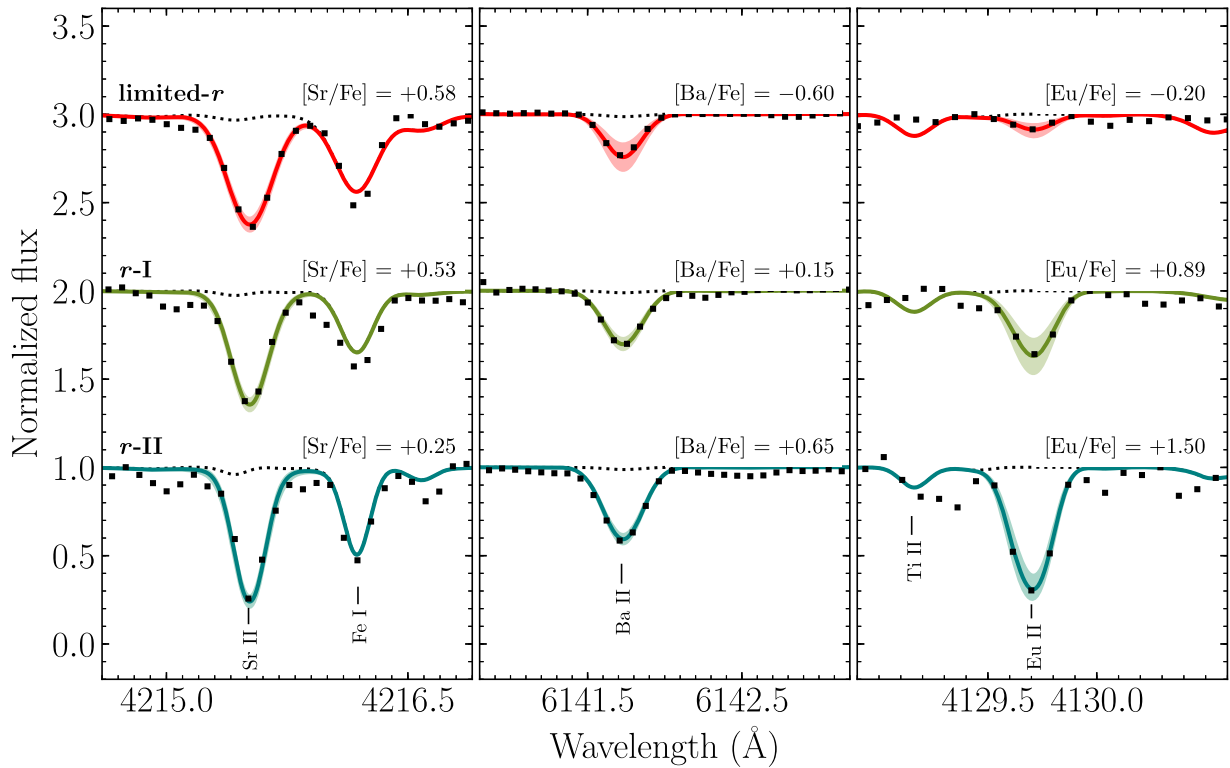


Figure 2. Syntheses of the Sr II 4215 Å (left), Ba II 6141 Å (middle), and Eu II 4129 Å (right) features for a limited-*r* star (J18121045–4934495; red, top), an *r*-I star (J15582962–1224344; green, middle), and an *r*-II star (J02462013–1518419; blue, bottom). Following the representative errors given in Table 6, the Sr II and Ba II syntheses are shown with a ± 0.30 dex uncertainty region and Eu II with a ± 0.20 dex uncertainty (filled). Dashed lines show syntheses lacking the respective element.

Travaglio et al. 2004; Honda et al. 2006; Jacobson et al. 2015). We find 20 stars with abundances satisfying our limited-*r* criteria (see Table 1), which is about half of the stars with low Eu abundances in our sample.

We note that four CEMP-*s* stars were also found in our sample, again because not all targets for this run had been through our eventual Phase-I vetting process.

5.2. Metallicity Distribution

Figure 3 shows the number of identified *r*-I, *r*-II, and limited-*r* stars as a function of metallicity. We detect both *r*-I and *r*-II stars over a wide metallicity range ($-3.0 \lesssim [\text{Fe}/\text{H}] \lesssim -1.5$). The limited-*r* stars are found primarily at the low-metallicity end; from $[\text{Fe}/\text{H}] \sim -2$ and down to $[\text{Fe}/\text{H}] \sim -3$. The observed distribution for the limited-*r* stars indicates that this signature is more clear in metal-poor environments, where chemical evolution has not yet erased signatures of individual processes, as opposed to more chemically evolved systems, in which only processes leaving a strong chemical signature can be identified anymore, like the *r*-II stars. However, the currently available sample remains small. With future, larger samples of *r*-I, *r*-II, and limited-*r* stars collected by the RPA, we will soon be able to better determine the metallicity distributions of these stars.

The metallicity distribution of our sample also differs from that of Barklem et al. (2005). The Barklem et al. (2005) stars have a median $[\text{Fe}/\text{H}] \sim -2.8$, after selecting candidates with $[\text{Fe}/\text{H}] \leq -2.5$. In contrast, we chose $[\text{Fe}/\text{H}] < -2.0$ for our initial candidate selection, and the median of our sample is $[\text{Fe}/\text{H}] \sim -2.4$. All of the *r*-II stars detected by Barklem et al. (2005) were found in a narrow metallicity range around $[\text{Fe}/\text{H}] \sim -3$, as do many of the *r*-II stars discovered since.

However, we detect *r*-II stars in a wider metallicity range, from $[\text{Fe}/\text{H}] = -3$ to $[\text{Fe}/\text{H}] = -1.5$, suggesting that the previous metallicity preference of these stars is likely an artifact or selection biases toward the overall lower metallicity in previous samples.

Interestingly, the metallicity distribution of the *r*-I and *r*-II stars found in the Milky Way satellites is more similar to what we find (Shetrone et al. 2001; Letarte et al. 2010). The one *r*-II star found in the bulge also has $[\text{Fe}/\text{H}] \sim -2$ (Johnson et al. 2013). Furthermore, we recently detected an *r*-II star with $[\text{Fe}/\text{H}] = -2$ in our northern hemisphere sample (Sakari et al. 2018).

Our sample also includes the most metal-rich *r*-II star detected in the Milky Way halo to date, J18024226–4404426, with $[\text{Fe}/\text{H}] = -1.55$, $[\text{Eu}/\text{Fe}] = +1.05$, and $[\text{Ba}/\text{Eu}] = -0.10$. The relatively high $[\text{Ba}/\text{Eu}]$ ratio found in J18024226–4404426 clearly shows that a substantial contribution from the *s*-process to the neutron-capture element abundances is present at this metallicity. Nevertheless, the neutron-capture-element abundance pattern of this star is dominated by the *r*-process, and, together with the other *r*-II stars discovered in this search, it widens the otherwise narrow metallicity distribution of the known *r*-II stars in the halo.

5.3. Magnitude Distribution

To demonstrate the difference in *V* magnitudes for our 10 newly discovered *r*-II stars compared to the literature sample *r*-II stars in the halo, we have plotted the number of *r*-II stars as a function of *V* magnitude in Figure 4 for our stars and the literature stars for which we could find *V* magnitudes. All of our new *r*-II stars have $V < 13$. Only four *r*-II stars this bright were known previously (J203843.2–002333, $V = 12.7$, Placco

Table 5
Abundances

Stellar ID	[Fe/H]	[C/Fe]	[Sr/Fe]	[Ba/Fe]	[Eu/Fe]	[Ba/Eu]	[Sr/Ba]	Subclass
J00002259–1302275	−2.90	−0.65	−1.20	−0.38	+0.58	−0.96	−0.82	<i>r</i> -I
J00021222–2241388	−2.19	−0.19	−0.13	−0.41	+0.22	−0.63	+0.28	...
J00021668–2453494	−1.81	−0.88	+0.59	+0.10	+0.52	−0.42	+0.49	<i>r</i> -I
J00133067–1259594	−2.82	−0.58	−0.25	−0.55	−0.06	−0.49	+0.30	...
J00233067–1631428	−2.45	+0.37	−0.75	−0.55	<+0.27	>−0.82	−0.20	Unknown
J00400685–4325183	−2.55	−0.85	−1.52	−1.56	+0.55	−2.11	+0.04	<i>r</i> -I
J00405260–5122491	−2.11	−0.04	+0.09	−0.04	+0.86	−0.90	+0.13	<i>r</i> -I
J00453930–7457294	−2.00	+0.93	+0.83	+0.37	+0.55	−0.18	+0.46	CEMP- <i>r</i>
J01202234–5425582	−2.11	−0.09	+0.50	+0.16	+0.30	−0.14	+0.34	<i>r</i> -I
J01293113–1600454	−2.81	+0.35	+0.88	+0.95	+1.76	−0.81	−0.07	<i>r</i> -II
J01334657–2727374	−1.60	+1.64	+1.40	+1.61	+0.88	+0.73	−0.21	CEMP- <i>s</i>
J01425422–5032488	−2.09	+0.07	+0.13	−0.13	+0.38	−0.51	+0.26	<i>r</i> -I
J01430726–6445174	−3.00	−0.14	−1.00	−0.51	−0.14	−0.37	−0.49	...
J01451951–2800583	−2.80	−0.69	+0.30	−0.98	<−0.38	>−0.60	+1.28	limited- <i>r</i>
J01490794–4911429	−2.94	+0.05	−0.45	−0.59	+0.09	−0.68	+0.14	...
J01530024–3417360	−1.50	+0.01	+0.40	+0.09	+0.71	−0.62	+0.31	<i>r</i> -I
J02040793–3127556	−3.08	−0.76	+0.07	−0.77	<+0.00	>−0.77	+0.84	limited- <i>r</i>
J02165716–7547064	−2.50	−0.33	+0.25	+0.25	+1.12	−0.87	+0.00	<i>r</i> -II
J02355867–6745520	−1.55	+0.97	+0.10	+0.49	+0.50	−0.01	−0.39	CEMP- <i>r</i>
J02401075–1416290	−0.79	+1.20	>+1.00	+1.69	+0.84	+0.85	>−0.69	CEMP- <i>s</i>
J02412152–1825376	−2.17	−0.96	+0.35	+0.09	+0.20	−0.11	+0.26	...
J02441479–5158241	−2.93	−0.05	−0.55	−0.80	+0.20	−1.00	+0.25	...
J02462013–1518419	−2.71	+0.04	+0.58	+0.60	+1.45	−0.85	−0.02	<i>r</i> -II
J02500719–5145148	−2.20	+1.04	−0.05	+0.48	+0.62	−0.14	−0.53	CEMP- <i>r</i>
J03193531–3250433	−2.93	<+1.60	−0.28	<−0.15	<+1.14	...	>−0.13	Unknown
J03563703–5838281	−2.87	−0.78	+0.55	−0.50	+0.11	−0.61	+1.05	limited- <i>r</i>
J04121388–1205050	−2.73	−0.12	+0.42	−0.43	+0.52	−0.95	+0.85	<i>r</i> -I
J13164824–2743351	−1.61	−0.05	+0.26	+0.01	+0.54	−0.53	+0.25	<i>r</i> -I
J14033542–3335257	−2.71	+0.08	+0.10	−0.28	+0.29	−0.57	+0.38	...
J14164084–2422000	−2.73	−0.86	+0.48	−0.44	+0.02	−0.46	+0.92	limited- <i>r</i>
J14232679–2834200	−1.90	+0.43	+0.44	−0.07	+0.61	−0.68	+0.51	<i>r</i> -I
J14301385–2317388	−1.40	−0.70	+0.40	+0.34	+0.62	−0.28	+0.06	<i>r</i> -I
J14325334–4125494	−2.79	−0.14	+0.32	+0.71	+1.61	−0.90	−0.39	<i>r</i> -II
J14381119–2120085	−2.21	+0.70	+0.42	+0.97	+0.62	+0.35	−0.55	...
J15260106–0911388	−2.83	−0.82	+0.90	+0.69	+1.70	−1.01	+0.21	<i>r</i> -II
J15271353–2336177	−2.15	+0.33	+0.35	−0.03	+0.70	−0.73	+0.38	<i>r</i> -I
J15575183–0839549	−1.49	+0.60	+1.20	+1.68	+0.70	+0.98	−0.48	...
J15582962–1224344	−2.54	−0.14	+0.53	+0.04	+0.89	−0.85	+0.49	<i>r</i> -I
J16024498–1521016	−1.80	−0.05	+0.35	+0.08	+0.55	−0.47	+0.27	<i>r</i> -I
J16080681–3215592	−2.07	−0.32	+0.07	+0.08	+0.25	−0.17	−0.01	...
J16095117–0941174	−2.82	−0.65	−0.10	−0.29	+0.17	−0.46	+0.19	...
J16103106+1003055	−2.43	+0.53	−0.19	−1.10	<+0.70	>−1.80	+0.91	Unknown
J16184302–0630558	−2.60	+0.40	−0.20	<−0.60	<+0.20	...	>+0.40	Unknown
J17093199–6027271	−2.47	−0.45	+0.28	−0.15	+0.60	−0.75	+0.43	<i>r</i> -I
J17094926–6239285	−2.51	−0.83	−0.05	−0.45	+0.02	−0.47	+0.40	...
J17124284–5211479	−2.78	−0.42	−0.03	−0.58	+0.48	−1.06	+0.55	<i>r</i> -I
J17225742–7123000	−2.42	−0.33	+0.31	+0.70	+1.07	−0.37	−0.39	<i>r</i> -II
J17255680–6603395	−2.59	−0.42	+0.04	−0.35	+0.18	−0.53	+0.39	...
J17273886–5133298	−1.78	−0.45	+0.12	+0.48	+0.48	+0.00	−0.36	...
J17285930–7427532	−2.04	−0.42	+0.74	−0.53	+0.23	−0.76	+1.27	limited- <i>r</i>
J17334285–5121550	−1.91	−0.32	+0.33	+0.19	+0.20	−0.01	+0.14	...
J17400682–6102129	−2.24	−0.26	+0.16	−0.31	+0.31	−0.62	+0.47	<i>r</i> -I
J17435113–5359333	−2.24	−0.35	+0.00	−0.07	+0.73	−0.80	+0.07	<i>r</i> -I
J18024226–4404426	−1.55	+0.35	+0.68	+0.95	+1.05	−0.10	−0.27	<i>r</i> -II
J18121045–4934495	−3.02	−0.33	+0.25	−0.50	−0.07	−0.43	+0.75	limited- <i>r</i>
J18285086–3434203	−2.46	−0.58	+0.22	−0.29	+0.53	−0.82	+0.51	<i>r</i> -I
J18294122–4504000	−2.48	−0.46	+0.47	−0.06	+0.70	−0.76	+0.53	<i>r</i> -I
J18362318–6428124	−2.57	+0.10	−0.63	+0.18	+0.57	−0.39	−0.81	<i>r</i> -I
J18363613–7136597	−2.52	−0.75	+0.01	−0.37	+0.56	−0.93	+0.38	<i>r</i> -I
J18562774–7251331	−2.26	−0.48	+0.00	−0.01	+0.32	−0.33	+0.01	<i>r</i> -I
J19014952–4844359	−1.87	+0.02	+0.37	−0.24	+0.93	−1.17	+0.61	<i>r</i> -I
J19161821–5544454	−2.35	−0.80	+0.48	−0.12	+1.08	−1.20	+0.60	<i>r</i> -II
J19172402–4211240	−2.44	−0.58	−0.13	−0.33	+0.11	−0.44	+0.20	...
J19173310–6628545	−2.76	−0.40	−0.35	−0.60	+0.00	−0.60	+0.25	...

Table 5
(Continued)

Stellar ID	[Fe/H]	[C/Fe]	[Sr/Fe]	[Ba/Fe]	[Eu/Fe]	[Ba/Eu]	[Sr/Ba]	Subclass
J19202070–6627202	–2.10	–0.28	+0.73	–0.11	+0.29	–0.40	+0.84	limited- <i>r</i>
J19215077–4452545	–2.56	–0.77	–0.05	–0.31	+0.74	–1.05	+0.26	<i>r</i> -I
J19232518–5833410	–2.08	+0.27	+0.56	+0.11	+0.76	–0.65	+0.45	<i>r</i> -I
J19324858–5908019	–1.93	–0.51	+0.90	+0.65	+0.90	–0.25	+0.25	<i>r</i> -I
J19345497–5751400	–2.46	–0.70	+0.25	–0.71	+0.17	–0.88	+0.96	limited- <i>r</i>
J19494025–5424113	–2.81	–0.55	–0.05	–1.01	–0.39	–0.62	+0.96	limited- <i>r</i>
J19534978–5940001	–2.79	–0.44	+0.25	–0.52	+0.04	–0.56	+0.77	limited- <i>r</i>
J19594558–2549075	–2.44	–0.70	+0.10	–0.50	+0.04	–0.54	+0.60	limited- <i>r</i>
J20093393–3410273	–1.99	–0.86	+0.59	+0.23	+1.32	–1.09	+0.36	<i>r</i> -II
J20144608–5635300	–1.92	+1.50	+0.98	+1.08	+0.92	+0.16	–0.10	CEMP- <i>s</i>
J20165357–0503592	–2.89	–0.12	–2.43	–1.10	<+0.00	>–1.10	–1.33	...
J20303339–2519500	–2.21	–0.65	+0.41	–0.29	+0.41	–0.70	+0.70	<i>r</i> -I
J20313531–3127319	–2.43	+0.10	+0.20	–0.79	<–0.30	>–0.49	+0.99	limited- <i>r</i>
J20445584–2250597	–2.30	–0.57	+0.40	–0.05	–0.09	+0.04	+0.45	...
J20492765–5124440	–2.47	–0.77	+0.13	–0.25	+0.58	–0.83	+0.38	<i>r</i> -I
J20514971–6158008	–1.87	+0.10	+0.28	–0.18	+0.43	–0.61	+0.46	<i>r</i> -I
J20542346–0033097	–2.78	–0.36	+0.86	–0.03	<+0.00	>–0.03	+0.89	limited- <i>r</i>
J20560913–1331176	–2.30	+0.00	+0.13	–0.56	+0.00	–0.56	+0.69	limited- <i>r</i>
J21023752–5316132	–2.44	–0.38	–0.42	–1.63	<+0.20	>–1.43	+1.21	limited- <i>r</i>
J21063474–4957500	–2.91	+0.52	–0.48	–0.20	+0.54	–0.74	–0.28	<i>r</i> -I
J21064294–6828266	–2.76	+0.53	+0.90	+0.52	+1.32	–0.80	+0.38	<i>r</i> -II
J21091825–1310062	–2.40	–0.28	+0.14	+0.12	+1.25	–1.13	+0.02	<i>r</i> -II
J21095804–0945400	–2.73	–0.45	+0.60	–0.12	+0.77	–0.89	+0.72	<i>r</i> -I
J21141350–5726363	–2.69	–0.10	–0.32	–0.94	<–0.40	>–0.54	+0.62	limited- <i>r</i>
J21152551–1503309	–2.06	–0.07	+1.93	+1.41	+0.73	+0.68	+0.52	...
J21162185–0213420	–2.23	–0.98	+0.57	+0.06	+0.49	–0.43	+0.51	<i>r</i> -I
J21224590–4641030	–2.96	–0.18	+0.25	+0.01	+0.90	–0.89	+0.24	<i>r</i> -I
J21262525–2144243	–2.81	–0.88	+0.37	–0.02	+0.58	–0.60	+0.39	<i>r</i> -I
J21291592–4236219	–2.48	–0.07	–0.25	–0.54	<–0.20	>–0.34	+0.29	Unknown
J21370807–0927347	–2.46	–0.50	+0.63	–0.61	+0.11	–0.72	+1.24	limited- <i>r</i>
J21513595–0543398	–2.46	–1.20	–0.30	–0.66	+0.02	–0.68	+0.36	...
J22021636–0536483	–2.75	+0.05	+0.15	–0.75	<–0.12	>–0.63	+0.90	limited- <i>r</i>
J22163596+0246171	–2.37	–0.10	+0.17	–0.27	+0.45	–0.72	+0.44	<i>r</i> -I
J22444701–5617540	–1.86	–0.43	+0.63	+0.77	–0.21	+0.98	–0.14	...
J22492756–2238289	–1.82	–0.08	+0.39	–0.43	+0.48	–0.91	+0.82	<i>r</i> -I
J22531984–2248555	–1.87	+0.89	+0.55	+1.01	+0.88	+0.13	–0.46	...
J22595884–1554182	–2.64	–0.86	+0.03	–0.58	<–0.30	>–0.28	+0.61	limited- <i>r</i>
J23022289–6833233	–2.64	+0.30	+0.15	–0.29	+0.61	–0.90	+0.44	<i>r</i> -I
J23044914–4243477	–2.43	–0.62	+0.48	–0.42	<+0.07	>–0.49	+0.90	limited- <i>r</i>
J23130003–4507066	–2.64	+0.28	–0.60	–0.65	<+0.05	>–0.70	+0.05	Unknown
J23265258–0159248	–3.13	–0.63	+0.07	+0.31	+0.69	–0.38	–0.24	<i>r</i> -I
J23310716–0223301	–2.28	+1.95	+0.53	+2.23	+2.09	+0.14	–1.70	CEMP- <i>s</i>
J23362202–5607498	–2.06	–0.05	>+1.00	+0.24	+1.14	–0.90	>+0.76	<i>r</i> -II

(This table is available in machine-readable form.)

et al. 2017; CS 31082–001, $V = 11.6$, Hill et al. 2002; HE 1523–0901, $V = 11.1$, Frebel et al. 2006; and J153830.9–180424, $V = 10.86$, Sakari et al. 2018).

This sample also includes the brightest *r*-II star detected in the Milky Way’s halo to date, J21091825–1310062, with $V = 10.7$, $[\text{Fe}/\text{H}] = -2.40$, $[\text{Eu}/\text{Fe}] = +1.25$, and $[\text{Ba}/\text{Eu}] = -1.13$. This star has one of the lowest $[\text{Ba}/\text{Eu}]$ ratios found in our sample, indicating a pure *r*-process origin for the neutron-capture elements seen in this star. Note that the second brightest *r*-II star was discovered in the northern search for *r*-process-enhanced stars conducted by the RPA (Sakari et al. 2018). As the present manuscript was being prepared, yet another *r*-II star, even brighter than either of the above two stars ($V = 10.1$), was identified from northern hemisphere snapshot spectroscopy with the McDonald 2.7 m telescope. A

portrait spectrum was also obtained, and is reported on by E. Holmbeck et al. (2018, in preparation). The brightness of the *r*-II stars in our sample means that we will be able to derive very complete neutron-capture-element abundance patterns for them, including thorium and possibly uranium, which is essential to distinguish between different *r*-process models. A number are sufficiently bright to be studied in the near-UV at high spectral resolution with the *Hubble Space Telescope*.

5.4. Sr, Ba, Eu as R-process Indicators

With the stellar-parameter range and S/N of this sample, we are able to detect Eu abundances in our stars down to $[\text{Eu}/\text{Fe}] \sim -0.2$. The distribution of Eu abundances for our sample stars as a function of metallicity is shown in Figure 5. For comparison, we have also included Eu measurements from the large sample of

Table 6
Uncertainties for Three Representative Stars in the Sample

Abundance	T_{eff} (± 150 K)	$\log g$ (± 0.3 dex)	$\sigma_{[\text{Fe}/\text{H}]}$ (dex)	ξ (± 0.3 dex)	σ_{rand} (dex)	σ_{tot} (dex)
J02500719–5145148 (4707/1.40/–2.20/2.30)						
[C/Fe]	± 0.30	± 0.04	± 0.21	± 0.01	± 0.05	± 0.37
[Sr/Fe]	± 0.15	± 0.08	± 0.21	± 0.22	± 0.05	± 0.35
[Ba/Fe]	± 0.12	± 0.13	± 0.21	± 0.24	± 0.05	± 0.37
[Eu/Fe]	± 0.13	± 0.08	± 0.21	± 0.02	± 0.05	± 0.26
J13164824–2743351 (4990/2.24/–1.61/1.50)						
[C/Fe]	± 0.28	± 0.09	± 0.18	± 0.04	± 0.05	± 0.35
[Sr/Fe]	± 0.08	± 0.08	± 0.18	± 0.05	± 0.05	± 0.22
[Ba/Fe]	± 0.08	± 0.14	± 0.18	± 0.24	± 0.05	± 0.34
[Eu/Fe]	± 0.07	± 0.12	± 0.18	± 0.07	± 0.05	± 0.24
J20514971–6158008 (5285/3.13/–1.87/1.68)						
[C/Fe]	± 0.28	± 0.03	± 0.15	± 0.01	± 0.05	± 0.32
[Sr/Fe]	± 0.13	± 0.09	± 0.15	± 0.07	± 0.05	± 0.23
[Ba/Fe]	± 0.09	± 0.09	± 0.15	± 0.09	± 0.05	± 0.22
[Eu/Fe]	± 0.08	± 0.11	± 0.15	± 0.03	± 0.05	± 0.21

Table 7
Radial Velocities from RAVE DR5 and our Data for Possible Binaries

Stellar ID	MJD	RV (km s^{-1})	RV _{err} (km s^{-1})	Ref.
J02040793–3127556	55866.62968	+89.0	0.5	RAVE DR5
	57607.90877	+83.4	1.0	this work
J02355867–6745520	54424.55569	+112.5	2.1	RAVE DR5
(<i>r</i> -I)	57610.82171	+101.5	0.2	this work
J02462013–1518419	55804.65655	+287.5	2.5	RAVE DR5
(<i>r</i> -II)	57609.92227	+278.2	0.4	this work
J17225742–7123000	55706.67402	+284.3	2.5	RAVE DR5
(<i>r</i> -II)	57605.55568	+277.3	0.5	this work
	57607.54850	+278.1	1.1	this work
J17400682–6102129	55441.36433	+262.4	0.5	RAVE DR5
(<i>r</i> -I)	57606.57576	+255.0	0.3	this work
J19534978–5940001	55687.77159	+209.3	1.5	RAVE DR5
(limited- <i>r</i>)	57608.66299	+216.4	0.6	this work
J20093393–3410273	54952.76815	+33.6	1.0	RAVE DR5
(<i>r</i> -II)	57607.68078	+27.2	0.3	this work
J21064294–6828266	55716.75769	–64.9	2.6	RAVE DR5
(<i>r</i> -II)	55738.76316	–71.6	18.7	RAVE DR5
	57608.73613	–72.7	0.6	this work
J22531984–2248555	53923.72365	+12.3	0.9	RAVE DR5
(CEMP- <i>s</i>)	57607.78387	–7.0	0.1	this work

Roederer et al. (2014a). Similar to Roederer et al. (2014a), we find a large spread (> 2 dex) in the Eu abundances derived for our sample. This spread has been interpreted as a possible sign of multiple production sites for *r*-process elements (Sneden et al. 2000; Travaglio et al. 2004). In particular, we are able to detect Eu in stars over the full metallicity range of our sample, indicating the need for a source of *r*-process elements early in the universe.

From Figure 5, it can also be seen that two of our identified limited-*r* stars have subsolar [Eu/Fe] abundances, a number of them cluster around around the solar value, and some are mildly enhanced in Eu. Our template star for the limited-*r* stars,

HD 122563, has subsolar [Sr/Fe], [Ba/Fe], and [Eu/Fe], and is thus *r*-element poor. We have chosen to include more stars in this group, requiring that they show lower Eu abundances than those of the *r*-I (and *r*-II) stars and larger abundances of the light *r*-process elements, compared to the heavy *r*-process elements ([Sr/Ba] $> +0.5$), as we wish to investigate the production of the light *r*-process elements with this group of stars.

The [Ba/Eu] ratio is often used as a diagnostic for the level of *r*- versus *s*-process origin of the neutron-capture elements measured in stars. Figure 6 shows the [Ba/Eu] ratios for our

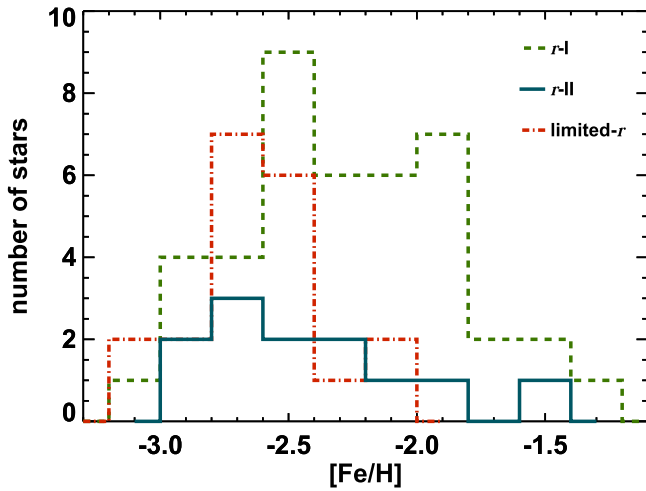


Figure 3. Histogram showing the number of detected r -I (dashed green line), r -II (solid blue line), and limited- r (dotted-dashed red line) stars in our sample (including duplicates), as a function of metallicity.

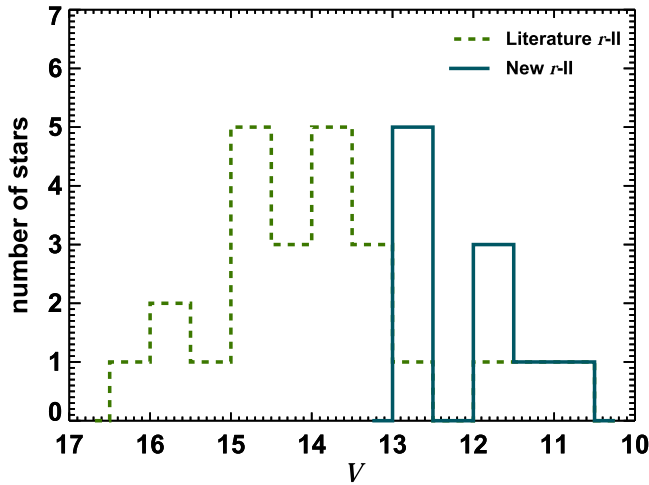


Figure 4. V magnitudes for the literature sample of halo r -II stars and the new r -II stars found in our sample (Rossi et al. 2005; Beers et al. 2007; Zacharias et al. 2012; Cohen et al. 2013; Munari et al. 2014; Roederer et al. 2014a).

sample stars, as a function of metallicity, along with the solar system r - and s -process ratios from Simmerer et al. (2004). The majority of our newly discovered r -II stars have $[\text{Ba}/\text{Eu}] < -0.8$, indicating a pure r -process origin for the neutron-capture-element content of these stars. The r -I and limited- r stars exhibit a larger variation in their $[\text{Ba}/\text{Eu}]$ values, slightly increasing with metallicity.

We also plot the absolute Eu abundances derived for our stars, as a function of metallicity, in Figure 7. A clear increase of Eu with Fe is seen for both the r -process-enhanced and non- r -process-enhanced stars; a similar trend is also seen for r -process-enhanced stars detected in dwarf galaxies (Hansen et al. 2017). The slopes for the r -I and r -II stars appear to differ in this plot, indicating different enrichment of these stars. It is likely that the sampling of r -I stars at the low-metallicity end is incomplete, due to the difficulty in detecting the lines for low Eu abundances in these stars. Also, the sampling of r -II stars at higher metallicity is sparse. Hence, the difference in slopes may

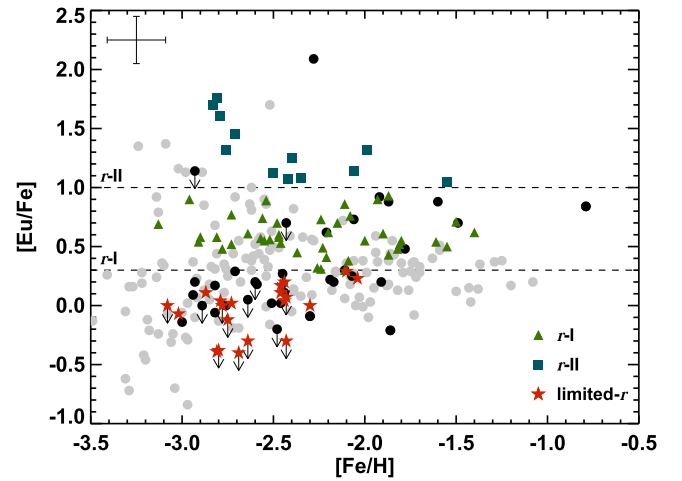


Figure 5. Derived $[\text{Eu}/\text{Fe}]$ abundances for the sample, as a function of metallicity: r -I stars (green triangles), r -II stars (blue squares), limited- r (red stars), and non- r -process-enhanced stars (black dots). The upper limits are shown with black arrows. For comparison, Eu measurements from Roederer et al. (2014a) are shown as gray dots. Division lines are drawn for non- r -process-enhanced, r -I, and r -II stars, shown with dashed lines at $[\text{Eu}/\text{Fe}] = +0.3$ and $+1.0$.

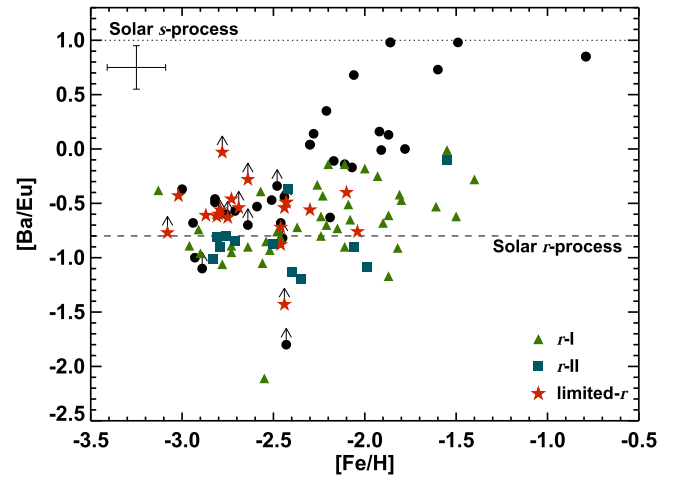


Figure 6. Derived $[\text{Ba}/\text{Eu}]$ abundances for the sample, as a function of metallicity: r -I stars (green triangles), r -II stars (blue squares), limited- r (red stars), and non- r -process-enhanced stars (black dots). The lower limits are shown with gray arrows. The dotted line is the solar system s -process fraction ($[\text{Ba}/\text{Eu}] = +1.0$) and the dashed line is the solar system r -process fraction ($[\text{Ba}/\text{Eu}] = -0.8$), both taken from Simmerer et al. (2004).

just be a result of the metallicity sampling difference. This will be easier to determine with future larger samples of r -I and r -II stars gathered by the RPA.

Finally, we plot the $[\text{Sr}/\text{Ba}]$ abundances, as a function of Eu abundance, in Figure 8. The limited- r stars cluster in the upper-left corner of this plot, showing higher abundances of the light r -process element Sr than the heavy r -process elements Ba and Eu. A few of the r -II and r -I also exhibit $[\text{Sr}/\text{Ba}] > +0.5$, but generally these stars have lower $[\text{Sr}/\text{Ba}]$ ratios than those of the limited- r stars.

6. Conclusions

This paper presents the first data sample from the southern hemisphere search for r -process-enhanced metal-poor stars in

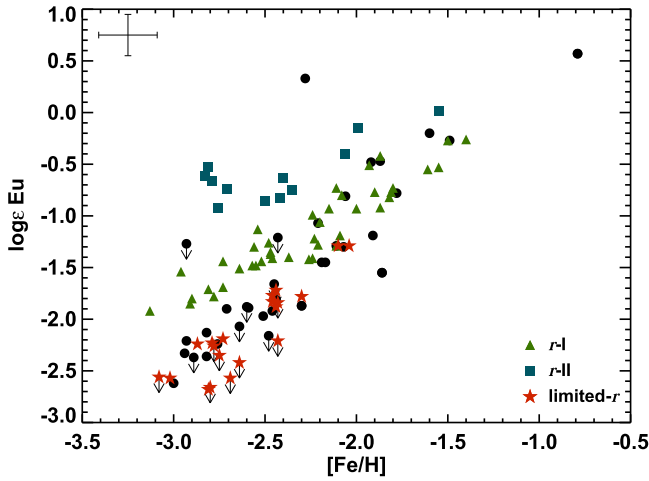


Figure 7. Absolute Eu abundances for the sample, as a function of metallicity: *r*-I stars (green triangles), *r*-II stars (blue squares), limited-*r* (red stars), and non-*r*-process-enhanced stars (black dots). The upper limits are shown with gray arrows.

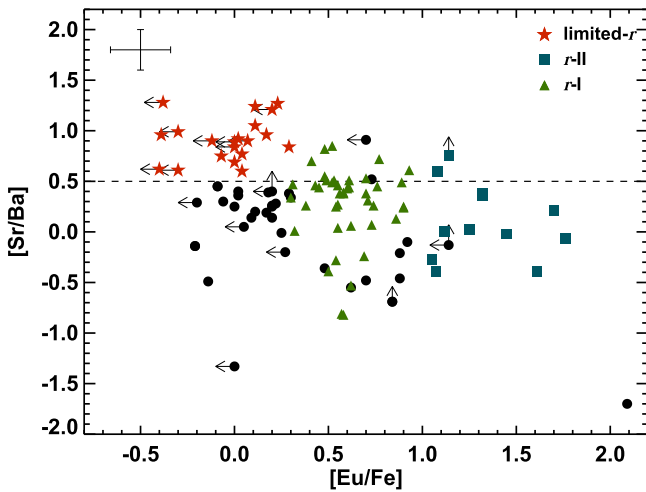


Figure 8. Derived [Sr/Ba] abundances for the sample, as a function of [Eu/Fe] abundances: *r*-I stars (green triangles), *r*-II stars (blue squares), limited-*r* (red stars), and non-*r*-process-enhanced stars (black dots). The limits are shown with black arrows and the dashed line marks [Sr/Ba] = +0.5.

the Galactic halo, conducted as part of the RPA in an effort to better understand the nature of the *r*-process. We have observed and analyzed a sample of 107 stars, identifying 10 new *r*-II stars (12 in total), 40 new *r*-I stars (42 in total, including the CEMP-*r* stars), and 20 new limited-*r* stars. Our sample has a wide metallicity range from $[\text{Fe}/\text{H}] = -3.13$ to -0.79 . While the majority of our newly discovered *r*-II stars are found at the metal-poor end of our sample, we identify these stars all the way up to $[\text{Fe}/\text{H}] = -1.5$. Specifically, in this sample we have detected the most metal-rich *r*-II star and the brightest *r*-II star known in the halo today. This metallicity distribution also agrees with that found for stars in dwarf galaxies, especially in the dwarf spheroidal galaxies. The *r*-I stars are detected at all metallicities as well, similar to what has been previously reported for these stars (Barklem et al. 2005). In this sample, we find limited-*r* stars only below $[\text{Fe}/\text{H}] \sim -2$. The low [Ba/Eu] ratios derived for the majority of our detected *r*-II stars suggests a pure *r*-process origin of the neutron-capture elements observed in these stars. The *r*-I and limited-*r* stars

exhibit higher [Ba/Eu], suggesting a more diluted and/or otherwise mixed neutron-capture-element content of their natal gas clouds, but still dominated by *r*-process material. Portrait spectra of the majority of the new *r*-II stars reported in this paper have been obtained, and analyses of these, which will enable us to identify possible actinide-boost stars, will be published in upcoming papers.

We thank the referee for helpful comments. This publication is based upon work supported in part by the National Science Foundation under grants AST-1108811 and AST-1714873. E.M.H., T.C.B., V.M.P., I.U.R., and A.F. acknowledge partial support from grant PHY 14-30152 (Physics Frontier Center/JINA-CEE), awarded by the U.S. National Science Foundation (NSF). A.F. is supported by NSF CAREER grant AST-1255160. C.M.S. acknowledges funding from the Kenilworth Fund of the New York Community Trust. This research has made use of NASA’s Astrophysics Data System Bibliographic Services.

Facility: du Pont.

Software: MOOG (Snedden 1973; Sobeck et al. 2011), IRAF (Tody 1986, 1993), linemake (<https://github.com/vmplacco/linemake>), ATLAS9 (Castelli & Kurucz 2003).

ORCID iDs

Terese T. Hansen <https://orcid.org/0000-0001-6154-8983>
 Erika M. Holmbeck <https://orcid.org/0000-0002-5463-6800>
 Timothy C. Beers <https://orcid.org/0000-0003-4573-6233>
 Vinicius M. Placco <https://orcid.org/0000-0003-4479-1265>
 Ian U. Roederer <https://orcid.org/0000-0001-5107-8930>
 Anna Frebel <https://orcid.org/0000-0002-2139-7145>
 Charli M. Sakari <https://orcid.org/0000-0002-5095-4000>

References

- Abazajian, K. N., Adelman-McCarthy, J. K., Agüeros, M. A., et al. 2009, *ApJS*, **182**, 543
- Abbott, B. P., Abbott, R., Abbott, T. D., et al. 2017, *PhRvL*, **119**, 161101
- Abohalima, A., & Frebel, A. 2017, arXiv:1711.04410
- Aoki, W., Honda, S., Sadakane, K., & Arimoto, N. 2007, *PASJ*, **59**, L15
- Arcones, A., Janka, H.-T., & Scheck, L. 2007, *A&A*, **467**, 1227
- Asplund, M., Grevesse, N., Sauval, A. J., & Scott, P. 2009, *ARA&A*, **47**, 481
- Barklem, P. S., Christlieb, N., Beers, T. C., et al. 2005, *A&A*, **439**, 129
- Beers, T. C., & Christlieb, N. 2005, *ARA&A*, **43**, 531
- Beers, T. C., Flynn, C., Rossi, S., et al. 2007, *ApJS*, **168**, 128
- Beers, T. C., Norris, J. E., Placco, V. M., et al. 2014, *ApJ*, **794**, 58
- Beers, T. C., Placco, V. M., Carollo, D., et al. 2017, *ApJ*, **835**, 81
- Beers, T. C., Preston, G. W., & Shectman, S. A. 1985, *AJ*, **90**, 2089
- Beers, T. C., Preston, G. W., & Shectman, S. A. 1992, *AJ*, **103**, 1987
- Brooke, J. S. A., Bernath, P. F., Schmidt, T. W., & Bacsikay, G. B. 2013, *JQSRT*, **124**, 11
- Burbidge, E. M., Burbidge, G. R., Fowler, W. A., & Hoyle, F. 1957, *RvMP*, **29**, 547
- Cameron, A. G. W. 1957, *PASP*, **69**, 201
- Cameron, A. G. W. 2003, *ApJ*, **587**, 327
- Castelli, F., & Kurucz, R. L. 2003, in IAU Symp. 210, Modelling of Stellar Atmospheres, ed. N. Piskunov, W. W. Weiss, & D. F. Gray (Cambridge: Cambridge Univ. Press), A20
- Christlieb, N., Beers, T. C., Barklem, P. S., et al. 2004, *A&A*, **428**, 1027
- Christlieb, N., Schörck, T., Frebel, A., et al. 2008, *A&A*, **484**, 721
- Cohen, J. G., Christlieb, N., Thompson, I., et al. 2013, *ApJ*, **778**, 56
- Cohen, J. G., & Huang, W. 2009, *ApJ*, **701**, 1053
- Cohen, J. G., & Huang, W. 2010, *ApJ*, **719**, 931
- Côté, B., Belczynski, K., Fryer, C. L., et al. 2017, *ApJ*, **836**, 230
- Demarque, P., Woo, J.-H., Kim, Y.-C., & Yi, S. K. 2004, *ApJS*, **155**, 667
- Dominik, M., Belczynski, K., Fryer, C., et al. 2012, *ApJ*, **759**, 52
- Drout, M. R., Piro, A. L., Shappee, B. J., et al. 2017, *Sci*, **358**, 1570
- Ezzeddine, R., Frebel, A., & Plez, B. 2017, *ApJ*, **847**, 142

- Frebel, A. 2018, ARNPS, submitted
- Frebel, A., Casey, A. R., Jacobson, H. R., & Yu, Q. 2013, *ApJ*, **769**, 57
- Frebel, A., Christlieb, N., Norris, J. E., et al. 2006, *ApJ*, **652**, 1585
- Frebel, A., Christlieb, N., Norris, J. E., et al. 2007, *ApJL*, **660**, L117
- Frebel, A., & Norris, J. E. 2015, *ARA&A*, **53**, 631
- Gallagher, A. J., Ryan, S. G., García Pérez, A. E., & Aoki, W. 2010, *A&A*, **523**, A24
- Gratton, R., Sneden, C., & Carretta, E. 2004, *ARA&A*, **42**, 385
- Gull, M., Frebel, A., Madelyn, G. C., Placco, V. M., et al. 2018, *ApJ*, submitted
- Hansen, C. J., Nordström, B., Hansen, T. T., et al. 2016, *A&A*, **588**, A37
- Hansen, T., Andersen, J., Nordstrom, B., Buchhave, L. A., & Beers, T. C. 2011, *ApJL*, **743**, L1
- Hansen, T. T., Andersen, J., Nordström, B., et al. 2015, *A&A*, **583**, A49
- Hansen, T. T., Simon, J. D., Marshall, J. L., et al. 2017, *ApJ*, **838**, 44
- Henden, A., & Munari, U. 2014, *CoSka*, **43**, 518
- Hill, V., Plez, B., Cayrel, R., et al. 2002, *A&A*, **387**, 560
- Honda, S., Aoki, W., Ishimaru, Y., Wanajo, S., & Ryan, S. G. 2006, *ApJ*, **643**, 1180
- Honda, S., Aoki, W., Kajino, T., et al. 2004, *ApJ*, **607**, 474
- Jacobson, H. R., Keller, S., Frebel, A., et al. 2015, *ApJ*, **807**, 171
- Ji, A. P., Frebel, A., Chiti, A., & Simon, J. D. 2016a, *Natur*, **531**, 610
- Ji, A. P., Frebel, A., Simon, J. D., & Chiti, A. 2016b, *ApJ*, **830**, 93
- Johnson, C. I., McWilliam, A., & Rich, R. M. 2013, *ApJL*, **775**, L27
- Kelson, D. D. 1998, PhD thesis, Univ. California at Santa Cruz
- Kelson, D. D. 2003, *PASP*, **115**, 688
- Kelson, D. D., Illingworth, G. D., van Dokkum, P. G., & Franx, M. 2000, *ApJ*, **531**, 159
- Kilpatrick, C. D., Foley, R. J., Kasen, D., et al. 2017, *Sci*, **358**, 1583
- Kordopatis, G., Gilmore, G., Steinmetz, M., et al. 2013, *AJ*, **146**, 134
- Kunder, A., Kordopatis, G., Steinmetz, M., et al. 2017, *AJ*, **153**, 75
- Lai, D. K., Bolte, M., Johnson, J. A., et al. 2008, *ApJ*, **681**, 1524
- Lattimer, J. M., & Schramm, D. N. 1974, *ApJL*, **192**, L145
- Lawler, J. E., Wickliffe, M. E., den Hartog, E. A., & Sneden, C. 2001, *ApJ*, **563**, 1075
- Letarte, B., Hill, V., Tolstoy, E., et al. 2010, *A&A*, **523**, A17
- Mashonkina, L., Christlieb, N., & Eriksson, K. 2014, *A&A*, **569**, A43
- Masseron, T., Plez, B., Van Eck, S., et al. 2014, *A&A*, **571**, A47
- Mösta, P., Roberts, L. F., Halevi, G., et al. 2017, arXiv:1712.09370
- Munari, U., Henden, A., Frigo, A., et al. 2014, *AJ*, **148**, 81
- Nishimura, N., Takiwaki, T., & Thielemann, F.-K. 2015, *ApJ*, **810**, 109
- Placco, V. M., Beers, T. C., Santucci, R. M., et al. 2018, *AJ*, submitted
- Placco, V. M., Holmbeck, E. M., Frebel, A., et al. 2017, *ApJ*, **844**, 18
- Ram, R. S., Brooke, J. S. A., Bernath, P. F., Sneden, C., & Lucatello, S. 2014, *ApJS*, **211**, 5
- Roederer, I. U., Cowan, J. J., Preston, G. W., et al. 2014b, *MNRAS*, **445**, 2970
- Roederer, I. U., Mateo, M., Bailey, J. I., III, et al. 2016, *AJ*, **151**, 82
- Roederer, I. U., Preston, G. W., Thompson, I. B., et al. 2014a, *AJ*, **147**, 136
- Rossi, S., Beers, T. C., Sneden, C., et al. 2005, *AJ*, **130**, 2804
- Rosswog, S., Korobkin, O., Arcones, A., Thielemann, F.-K., & Piran, T. 2014, *MNRAS*, **439**, 744
- Sakari, C. M., Placco, V. M., Hansen, T., et al. 2018, *ApJL*, **854**, L20
- Schlaufman, K. C., & Casey, A. R. 2014, *ApJ*, **797**, 13
- Shappee, B. J., Simon, J. D., Drout, M. R., et al. 2017, *Sci*, **358**, 1574
- Shetrone, M., Venn, K. A., Tolstoy, E., et al. 2003, *AJ*, **125**, 684
- Shetrone, M. D., Côté, P., & Sargent, W. L. W. 2001, *ApJ*, **548**, 592
- Simmerer, J., Sneden, C., Cowan, J. J., et al. 2004, *ApJ*, **617**, 1091
- Siqueira Mello, C., Hill, V., Barbay, B., et al. 2014, *A&A*, **565**, A93
- Sneden, C., Cowan, J. J., Ivans, I. I., et al. 2000, *ApJL*, **533**, L139
- Sneden, C., Lucatello, S., Ram, R. S., Brooke, J. S. A., & Bernath, P. 2014, *ApJS*, **214**, 26
- Sneden, C., & Parthasarathy, M. 1983, *ApJ*, **267**, 757
- Sneden, C., Preston, G. W., McWilliam, A., & Searle, L. 1994, *ApJL*, **431**, L27
- Sneden, C. A. 1973, PhD thesis, The Univ. Texas
- Sobeck, J. S., Kraft, R. P., Sneden, C., et al. 2011, *AJ*, **141**, 175
- Thanathibodee, T. 2016, Chemical Abundance Analysis of HE 2324-0215, an r-process-enhanced Metal-poor Star, Massachusetts Institute of Technology, <http://hdl.handle.net/1721.1/105644>
- Thielemann, K. F., Eichler, M., Panov, I. V., & Wehmeyer, B. 2017, *ARNPS*, **67**, 253
- Tody, D. 1986, *Proc. SPIE*, **627**, 733
- Tody, D. 1993, in ASP Conf. Ser. 52, Astronomical Data Analysis Software and Systems II, ed. R. J. Hanisch, R. J. V. Brissenden, & J. Barnes (San Francisco, CA: ASP), **173**
- Travaglio, C., Gallino, R., Arnone, E., et al. 2004, *ApJ*, **601**, 864
- Tsujimoto, T., Matsuno, T., Aoki, W., Ishigaki, M. N., & Shige-yama, T. 2017, *ApJL*, **850**, L12
- Wanajo, S. 2013, *ApJL*, **770**, L22
- Winteler, C., Käppeli, R., Perego, A., et al. 2012, *ApJL*, **750**, L22
- Wolf, C., Onken, C. A., Luvaul, L. C., et al. 2018, *PASA*, **35**, e010
- Yanny, B., Rockosi, C., Newberg, H. J., et al. 2009, *AJ*, **137**, 4377
- Zacharias, N., Finch, C. T., Girard, T. M., et al. 2012, *yCat*, **1322**, 0